THE JOURNAL OF PHYSICAL CHEMISTRY B

Article

pubs.acs.org/JPCB

SAFT-γ Force Field for the Simulation of Molecular Fluids: 2. Coarse-Grained Models of Greenhouse Gases, Refrigerants, and Long Alkanes

Carlos Avendaño,[†,‡] Thomas Lafitte,[†,§] Claire S. Adjiman,[†] Amparo Galindo,[†] Erich A. Müller,[†] and George Jackson*[,†]

[†]Department of Chemical Engineering, Centre for Process Systems Engineering, Imperial College London, South Kensington Campus, London SW7 2AZ, United Kingdom

[‡]School of Chemical Engineering and Analytical Science, The University of Manchester, Sackville Street, Manchester M13 9PL, United Kingdom

[§]Department of Chemical and Biochemical Engineering, The University of Sheffield, Mappin Street, Sheffield S1 3JD, United Kingdom

ABSTRACT: In the first paper of this series [C. Avendaño, T. Lafitte, A. Galindo, C. S. Adjiman, G. Jackson, and E. A. Müller, *J. Phys. Chem. B* **2011**, *115*, 11154] we introduced the SAFT-γ force field for molecular simulation of fluids. In our approach, a molecular-based equation of state (EoS) is used to obtain coarse-grained (CG) intermolecular potentials that can then be employed in molecular simulation over a wide range of thermodynamic conditions of the fluid. The macroscopic experimental data for the vapor−liquid equilibria (saturated liquid density and vapor pressure) of a given system are represented with the SAFT-VR Mie EoS and used to estimate effective intermolecular parameters that provide a good description of the thermodynamic properties by exploring a wide parameter space for models based on the Mie (generalized Lennard-Jones) potential. This methodology was first used to develop a simple single-segment CG Mie model of carbon dioxide (CO_2) which allows for a reliable representation of the fluid-phase equilibria (for which the model was parametrized), as well as an accurate prediction of other properties such as the enthalpy of vaporization, interfacial tension, supercritical density, and second-derivative thermodynamic properties (thermal expansivity, isothermal compressibility, heat capacity, Joule-Thomson coefficient, and speed of sound). In our current paper, the methodology is further applied and extended to develop effective SAFT-γ CG Mie force fields for some important greenhouse gases including carbon tetrafluoride (CF_4) and sulfur hexafluoride (SF_6), modeled as simple spherical molecules, and for long linear alkanes including *n*-decane (n-$C_{10}H_{22}$) and *n*-eicosane (n-$C_{20}H_{42}$), modeled as homonuclear chains of spherical Mie segments. We also apply the SAFT-γ methodology to obtain a CG homonuclear two-segment Mie intermolecular potential for the more challenging polar and asymmetric compound 2,3,3,3-tetrafluoro-1-propene (HFO-1234yf), a novel replacement refrigerant with promising properties. The description of the fluid-phase behavior and the prediction of the other thermophysical properties obtained by molecular simulation using our SAFT-γ CG Mie force fields are found to be of comparable quality (and sometimes superior) to that obtained using the more sophisticated all-atom (AA) and united-atom (UA) models commonly employed in the field. We should emphasize that though the focus of our current work is on simple homonuclear models, the SAFT-γ methodology is based on a group contribution methodology which is naturally suited to the development of more sophisticated heteronuclear models.

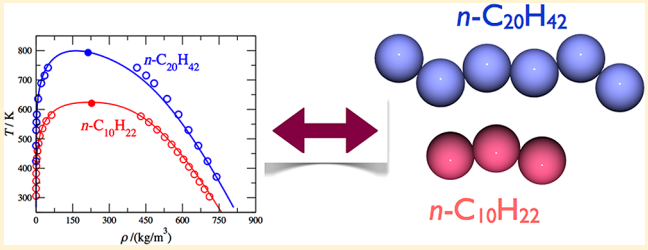

I. INTRODUCTION

An accurate description of the thermophysical and structural properties of complex molecular systems and soft materials using molecular modeling methods is of ubiquitous importance in physical, engineering, and material science.[1] Progress in the development of simulation methods for use in chemical engineering applications has been reviewed in recent years.[2−4] Depending on the length and time scales required for the computation of the desired properties, different techniques and levels of resolution can be employed. If the properties of the system under study depend on the distribution of subatomic particles, like electrons and protons, the system then lies in the realm of quantum mechanics, and one has to solve (in an approximate manner) the Schrödinger equation using, for example, traditional *ab initio* methods or density functional theory (DFT).[5] However, the high level of resolution of these methods can be avoided if the precise details of the electronic structure do not play a direct role in determining the macroscopic properties of the system at larger scales. It should also be pointed out that even with the most sophisticated

Received: June 29, 2012
Revised: January 8, 2013
Published: January 12, 2013

quantum mechanical description, an accurate determination of fluid-phase equilibria, which turns out to be very sensitive to the precise nature of the dispersion interactions, is still a near-insurmountable challenge (e.g., see the work on a first-principles representation of the equilibrium properties of water,[6−9] carbon dioxide,[10] methane, and methanol[11]). Alternatively, the electronic degrees of freedom can be averaged out to model the material as formed by atoms or molecules described within classical or semiclassical statistical mechanics.[12,13] Classical atomistic simulation is now well established in the form of Monte Carlo and molecular dynamics techniques,[14−18] and has been used to explore and understand the behavior of simple and complex molecules on time scales extending over hundreds of nanoseconds.[19,20] The development of more sophisticated force fields and more efficient numerical algorithms, together with the accessibility of much faster computers, has made it possible to use atomistic simulation as a routine technique for the description of the properties of matter.[3]

Notwithstanding the importance of atomistic simulations, many interesting and important phenomena in soft matter, such as the self-assembly of large complex molecules, protein folding, or colloidal aggregation, are typically observed in the mesoscopic regime, which cannot be easily accessed with atomistic approaches.[20] Coarse-graining (CG) methodologies are increasingly being used to span the gap between the atomistic and mesoscopic representations of matter, and play a primary role in helping to improve our understanding of the behavior of complex systems. In CG methods, the systems under study are represented at a lower level of resolution, while still retaining an appropriate description of the target properties of interest. The degrees of freedom characterizing the atomistic or quantum models that are not relevant in the large-scale regime can then either be ignored altogether or subsumed into effective interactions between bundles of matter (superatoms) formed by combining several atoms or functional groups.[3] There are a number of excellent reviews of the different methodologies and features relevant to CG approaches,[19,21−25] a clear attestation that CG techniques are now firmly established in their own right.[26]

The most common CG methodology involves a "bottom-up" approach in which thermodynamic properties and/or structural information obtained from scattering experiments or high-resolution simulations (all-atom or quantum mechanical calculations) are used to obtain simplified models appropriate for large-scale simulation.[21,26,27] Bottom-up CG approaches of this type include iterative Boltzmann inversion (IBI)[21,27,28] and force matching (FM) methods.[24,26,29−31] In the IBI approach, structural distribution functions are used to derive inter- and intramolecular pair interactions by means of the uniqueness theorem for the pair correlation functions.[32,33] The CG interactions obtained with such a procedure are strictly only applicable for the thermodynamic state in question, leading to problems in transferability for different conditions. Alternatively, with the FM method the effective pairwise interactions are obtained by minimizing the difference between the forces acting on the CG sites and the corresponding forces of the underlying atomistic system. The CG forces are represented using a predetermined functional form, which can be optimized during the minimization. A different CG methodology in multiscale modeling was introduced by Shell and co-workers,[34,35] where the so-called relative entropy is used as a metric to quantify the extent of overlap between the probability distributions of the models at different scales. The relative entropy can be used to develop CG models by reproducing the properties of a target high-resolution model.

The issue of transferability of the CG intermolecular potential to different thermodynamic states or to related molecular systems is still a challenge. Group contribution approaches, in which molecules are represented as assemblies of chemically distinct functional groups which interact in the same way regardless of the system, have been developed to address the latter issue. The MARTINI force field introduced by Marrink and co-workers[36] (for biomolecular systems) and the CG force-fields introduced by Klein and co-workers[37−40] (that have been used to model systems of varying complexity such as alkanes, aromatic molecules, amino acids, and other biomolecules) are in essence a group contribution description. Other recent examples of the use of the group contribution concept include the work of Chiu et al.[41] and the CG version of the TraPPE force field (TraPPE-CG) developed by Maerzke and Siepmann.[42] Different functional forms are used for the nonbonded interactions in these CG force fields: in the MARTINI force field, the nonbonded interactions are parametrized with a simple Lennard-Jones (LJ) 12−6 potential.[43,44] More flexible functional forms such as the Morse[45] (anharmonic exponential) or Mie[46] (generalized LJ) potentials have been used in other approaches, allowing for a control of the balance between the repulsive and attractive interactions.

These CG methodologies have been applied to describe broad classes of complex systems with varying degrees of success. It is nevertheless clear that the development of new robust approaches enabling an efficient determination of CG models that can be used with confidence for different macroscopic thermodynamic states still remains a considerable challenge in molecular modeling. Recently,[47] we introduced a coarse-graining methodology in which a molecular-based equation of state (EoS) of the statistical associating fluid theory (SAFT) family[48,49] is used as a link between experimental data for the fluid-phase equilibria and the parametrization of novel CG force fields based on the versatile Mie form. The SAFT description is based on Wertheim's[50−56] first-order thermodynamic perturbation theory (TPT1) for associating fluids. In the generic SAFT formulation, the thermodynamic properties of nonassociating chain molecules formed from m_s monomeric segments can be expressed in terms of the separate contribution due to the monomer segments, and the contribution due to the formation of chains of segments. The reader is directed to reviews of the SAFT methodology,[57−60] where details of the various versions of the theory are outlined with numerous examples of the successful application of the EoS for the description of the fluid-phase behavior and other thermodynamic properties of a wide variety of systems. In our work, we use the latest version of the theory for potentials of variable range (SAFT-VR). The SAFT-VR approach was originally developed to describe chains of square-well, Yukawa, or Lennard-Jones segments,[61−64] and later extended to the Mie potential.[65] The SAFT-VR EoS has now been enhanced to provide an improved description of the near-critical fluid region of molecules formed from Mie segments for systems characterized by differing values of the repulsive and attractive exponents and chain lengths.[66] The Mie potential offers a mathematical form that is more flexible than that of the Lennard-Jones potential; this is particularly advantageous in the development of CG models as both the softness/hardness of the repulsion and the range of the attraction between segments

can be varied independently. Hereafter, we refer to the latest incarnation of the theory[66] as SAFT-VR Mie and the coarse-grained models generated from it as the SAFT-γ CG Mie force field; SAFT-γ refers to the more generic group-contribution version of the approach for heteronuclear molecules formed from fused segments of different types (sizes and interactions).[67−69] The full development of the SAFT-VR Mie approach together with an assessment of the adequacy of the separate contributions to the free energy by judicious comparison with molecular simulation data for suitable model systems can be found in ref 66, with a summary of the key expressions presented in the Appendix of this paper for completeness.

The efficient development of accurate CG force fields using the SAFT-VR Mie EoS was first exemplified with the representation of the carbon dioxide (CO_2) molecule as a single Mie spherical CG segment.[47] Despite its simplicity, the resulting SAFT-γ CG Mie force field for CO_2 was shown to provide an excellent description of the vapor−liquid coexistence envelope, vapor pressure, compressed liquid density, interfacial tension, and second-derivative thermodynamic properties (including the coefficient of thermal expansion, isothermal compressibility, heat capacity, Joule-Thomson coefficient, and speed of sound). A significant advantage of employing a simple CG single-site model of CO_2 is that the corresponding molecular simulations are 2 to 3 orders of magnitude faster than with the more detailed multisite distributed charge all-atom (AA) or united-atom (UA) models that are in common use.[47]

A similar philosophy of coupling the development of intermolecular parameters from an algebraic SAFT-like EoS with molecular simulation was employed early on by Müller and Gubbins[70] who used an accurate representation of the LJ fluid together with dipolar[71] and associative[50−55] contributions to obtain a model for water; the adequacy of their approach is limited by the deteriorating accuracy of the theory for low-temperature, high-density states and in the neighborhood of the critical region. More recently, van Westen et al.[72] used the perturbed-chain version of SAFT (PC-SAFT[73]) to guide the development of force fields for the linear alkanes based on LJ segments. The PC-SAFT EoS was employed to approximate an objective function quantifying the deviations of the vapor pressure, enthalpy of vaporization, and saturated liquid density from the experimental values. The intermolecular potential parameters could thus be estimated by optimizing the description using the PC-SAFT thermodynamic properties, providing a good initial approximation of the force field. An iterative molecular simulation procedure was then used to determine an accurate set of intermolecular potential parameters. In the case of *n*-alkanes described as chains of LJ segments, the PC-SAFT model was found to provide a description of comparable accuracy to that obtained using well-established united-atom force fields such as TraPPE,[74] with an improved representation of the saturated vapor density and internal energy of vaporization. Though a direct link between the precise intermolecular potential model and the macroscopic thermodynamic properties is lost in the development of the PC-SAFT EoS,[73] the description allows one to capture essential information about the size and nonsphericity of the molecules and the integrated energy of the attractive interactions between the segments. However, the approximations inherent in the procedure necessitate the use of adjustable parameters for the segment size (molecular volume) and for the well depth (integrated energy) which have to be obtained iteratively by comparison with simulation. In generalizations of the approach to other forms of interaction such as the Mie or Buckingham (exponential-6) potentials, the adjustable parameters are expected to exhibit a temperature dependence[72] which may lead to some complications in the development of transferable models. By contrast, an explicit relationship between the intermolecular parameters of chain molecules formed from Mie segments and the macroscopic thermodynamic properties is retained in the formulation of the SAFT-VR Mie EoS,[47,66] obviating the need for this type of iterative simulation scheme; as we will show, a simple scaling of two parameters can be made for the more complex molecules where necessary by comparison to a single set of simulated data.

In order to demonstrate the generic nature of our procedure for the development of CG force fields using the SAFT-VR EoS,[66] we now obtain single-segment SAFT-γ CG Mie force fields for carbon tetrafluoride (CF_4) and sulfur hexafluoride (SF_6), which belong to the important class of molecules commonly referred to as greenhouse gases. This represents a stringent assessment of the adequacy of our intermolecular potential models, as the thermodynamic properties of perfluorinated compounds are typically very difficult to describe accurately with potentials of the traditional LJ 12−6 form.[75,76] For completeness, we include a comparison of the description obtained with the single-segment SAFT-γ CG Mie model for CO_2 reported in our previous work.[47] A homonuclear two-segment SAFT-γ CG Mie force field is also developed in our current paper for 2,3,3,3-tetrafluoro-1-propene (HFO-1234yf), a molecule with promising potential as a novel refrigerant;[77] the high polarity and polarizability of this partly fluorinated and unsaturated compound provides an additional test of the versatility of the simple SAFT-γ Mie force fields for asymmetric molecules. The extension of our CG methodology for highly nonspherical molecules is then exemplified with the development of SAFT-γ CG force fields for long linear alkanes, namely, *n*-decane (*n*-$C_{10}H_{22}$) and *n*-eicosane (*n*-$C_{20}H_{42}$), which are represented here as homonuclear chains of tangent Mie segments. In this case, one can use an additional scaling scheme for the model parameters using a single set of simulated data which allows for a significant improvement in the representation of the vapor−liquid equilibrium properties, particularly the low values of the vapor pressures which are commonly a challenge to describe for long-chain molecules of this type.

As we have already mentioned, the Mie form can be used instead of the more common Lennard-Jones potential to provide a better description of the thermophysical properties and phase equilibria of complex fluids in both atomistic and CG simulations. For example, Nielsen et al.[38] have developed a CG model based on the Mie potential for *n*-alkanes parametrized to reproduce surface tension data. In this case, each CG site is taken to represent approximately three carbon atoms interacting through a Mie potential with a softer repulsive contribution than that of the LJ potential. Using the same approach, Du et al.[76] obtained a CG model for the simulation of mixtures of perfluoroalkanes in supercritical CO_2. Gordon[78] has taken advantage of the tunability of the softness/hardness of the repulsive interactions with potentials of the Mie form to develop an accurate UA force field for the simultaneous representation of the transport and thermodynamic properties of *n*-alkanes, showing that TraPPE models based on the LJ form lead to a significant underprediction of the viscosity.

dx.doi.org/10.1021/jp306442b | J. Phys. Chem. B 2013, 117, 2717−2733

Despite its apparent simplicity, water always presents a challenge in molecular modeling at all levels of resolution. The Mie potential is being used with increasing popularity to represent water as simple one-segment models that are appropriate for the simulation of biomolecular systems. He et al.,[79] for example, have studied CG models of water in which a few water molecules (between one and four) are combined into a single Mie segment to reproduce different properties of liquid water, including the density, interfacial tension, and compressibility. These models of water have been simulated together with CG models for lipids and aromatic molecules by Shinoda et al.[39,80] and Devane et al.[81] An appropriate description of the softness/hardness of the repulsion and the range of the attractions between the water molecules is found to be important in preventing the system from freezing at ambient conditions, and in providing a good description of the compressibility and interfacial tension. This is also true for the models of the lipid molecules where the different repulsive and attractive exponents characterizing the molecules have to be adjusted to provide the best overall description of the structural and thermodynamic properties.[82] Maerzke and Siepmann[42] have recently reported a CG model for linear alkanes based on the UA TraPPE description,[74] where the bonded interactions were obtained through a IBI scheme using correlation functions determined from simulations of the TraPPE force field; the nonbonded interactions were modeled using different CG Mie segments. At the more detailed atomistic level, the Mie potential has been used by Potoff and Bernard-Brunel[75] to develop a UA force field based on the Mie potential to describe the fluid-phase equilibria of alkanes and perfluoroalkanes with great accuracy. These examples highlight how an appropriate choice of the repulsive (softness/hardness) and attractive (range of dispersion) contribution is of key importance in molecular modeling of fluids of varying complexity, particularly at higher levels of coarse graining.

The current paper is part of a series of contributions on the efficient development of novel SAFT-γ force fields for homonuclear or heteronuclear CG models formed from CG segments interacting through a Mie potential. Here, we demonstrate the adequacy and versatility of the SAFT-γ CG force fields in representing the thermodynamic and fluid-phase equilibria of systems of varying complexity including spherical models of the polarizable perfluorinated molecules CF_4 and SF_6, a homonuclear dimer model of the highly asymmetric and polar refrigerant HFO-1234yf, and homonuclear chain models of the highly nonspherical hydrocarbons n-$C_{10}H_{22}$ and n-$C_{20}H_{42}$.

II. ESTIMATION OF PARAMETERS FOR SAFT-γ FORCE FIELDS

II.1. General Approach. The methodology used in the current paper is based on a "top-down" approach recently proposed by our group. Here, one of the latest generations of the SAFT EoS[48,49] is used as the link between the experimental macroscopic properties of the fluid and the effective CG interactions.[47] We employ an extension of the generic SAFT methodology for potentials of variable range (SAFT-VR)[61,62,65,66,83,84] for molecules made up of segments interacting through the Mie[46] (generalized Lennard-Jones) potential, u^{Mie}, which can be expressed as[43,44,46]

$$u^{\mathrm{Mie}}(r) = C\varepsilon\left[\left(\frac{\sigma}{r}\right)^{\lambda_r} - \left(\frac{\sigma}{r}\right)^{\lambda_a}\right] \tag{1}$$

where r is the intersegment center-center distance, ε the potential well depth, σ the segment diameter, and λ_r and λ_a are parameters controlling the softness/hardness of the repulsion and the range of the attraction of the intermolecular potential, respectively. The constant C is defined as

$$C = \frac{\lambda_r}{\lambda_r - \lambda_a}\left(\frac{\lambda_r}{\lambda_a}\right)^{\lambda_a/(\lambda_r-\lambda_a)} \tag{2}$$

which ensures that the minimum of the potential is $-\varepsilon$. The key to the construction of the SAFT-γ force field is the determination of the intermolecular parameters of the m_s Mie segments making up the molecules. The four parameters in eq 1 are estimated from experimental fluid-phase equilibrium data for different substances by using the SAFT-VR Mie EoS[66] (see the Appendix of our current paper for a summary of the expressions).

A rigorous methodology to link the experimental thermodynamic properties and the theoretical representation for a model at any level of resolution is to match the free energy of the system for each thermodynamic state. Instead of the Helmholtz free energy, it is more practical to employ readily accessible thermodynamic properties such as the pressure (the volume derivative of the Helmholtz free energy) and the density in the estimation of the intermolecular parameters; the use of such properties at coexistence also implies a consideration of the chemical potential (the derivative of the free energy with respect to the particle number). As is common in engineering practice, we consider the minimization of unweighted least-squares residuals of the experimental and theoretical values for the chosen properties over a wide range of states by means of the following objective function:

$$\begin{aligned}\min_{\sigma,\varepsilon,\lambda_r,\lambda_a,m_s} & F_{\mathrm{obj,exp}}(\sigma, \varepsilon, \lambda_r, \lambda_a, m_s) \\ = \min_{\sigma,\varepsilon,\lambda_r,\lambda_a,m_s} & \left\{\sum_{i=1}^{N_p}\left(\frac{P_v^{\mathrm{SAFT}}(T_i; \sigma, \varepsilon, \lambda_r, \lambda_a, m_s) - P_v^{\mathrm{exp}}(T_i)}{P_v^{\mathrm{exp}}(T_i)}\right)^2\right. \\ & \left. + \sum_{j=1}^{N_\rho}\left(\frac{\rho_l^{\mathrm{SAFT}}(T_j; \sigma, \varepsilon, \lambda_r, \lambda_a, m_s) - \rho_l^{\mathrm{exp}}(T_j)}{\rho_l^{\mathrm{exp}}(T_j)}\right)^2\right\}\end{aligned} \tag{3}$$

where N_p and N_ρ are the number of experimental points for the vapor (saturation) pressure P_v and the saturated liquid density ρ_l, respectively. In this way, one is imposing an optimal correspondence between the theoretical and experimental derivatives of the Helmholtz free energy averaged over a range of temperatures T. Unless otherwise stated, the experimental data for the fluids examined in our work are obtained from the NIST database.[85] One should note that $F_{\mathrm{obj,exp}}$ is a function of the five interaction parameters of the Mie potential including the repulsive and attractive exponents λ_r and λ_a, as well as the number of segments m_s. Although the number of segments could generally be obtained from the estimation procedure, here we set it to a fixed integer to simplify the process, effectively controlling the level of coarse graining. It is also important to point out that though here only experimental vapor−liquid equilibrium data are used during the estimation procedure, there is no restriction to the breadth of

dx.doi.org/10.1021/jp306442b | J. Phys. Chem. B 2013, 117, 2717−2733

thermodynamic properties that can be considered. Thermodynamic derivative properties such as the Joule-Thomson coefficient, speed of sound, compressibility, and heat capacity could also be taken into account during the development of the force field. This capability is a particular advantage of using the SAFT-VR Mie EoS as it is found to provide an excellent representation of the second derivative properties of real substances.[65,66] This is one of the major strengths of our "top-down" CG methodology as it makes it possible to explore the force-field parameter space over a very wide range of thermodynamic conditions, something which is difficult to undertake with the more common "bottom-up" approaches. Since the SAFT-VR Mie EoS provides an excellent description of the thermodynamic properties of molecules formed from segments interacting via the Mie potential[66] (a well-defined Hamiltonian function), the CG parameters can be used as effective (averaged) intermolecular potentials in conventional molecular simulation. As mentioned in the Introduction, the approach has already been used and tested in the development of an accurate single-segment SAFT-γ CG Mie force field for the vapor−liquid equilibria (VLE) and second-derivative properties of CO_2.[47] We now extend the CG methodology to more complex systems with higher polarizability such as the halogenated greenhouse gases, and highly nonspherical molecules such as *n*-decane and *n*-eicosane. The alkane molecules are modeled as fully flexible chains of tangent coarse-grained segments, connected using rigid bonds so that internal degrees of freedom are not taken into account. The SAFT-γ CG Mie force-field parameters for the molecules studied in this work are listed in Table 1. In the case of the *n*-alkanes, the diameter and well depth of the segment−segment interactions can be scaled to provide an improved description of the vapor-pressure curve by employing a simple scaling analysis of the difference between the simulated and experimental data with the SAFT-VR Mie EoS. Details of the scaling are provided in the following section.

Table 1. SAFT-γ CG Mie Force-Field Parameters for the Molecules Studied in Our Current Work[a]

molecule	m_s	(ε/k_B)/K	σ/Å	λ_r	λ_a
CO_2	1	361.69	3.741	23.00	6.66
CF_4	1	265.57	4.350	32.53	6.00
SF_6	1	440.49	4.861	19.02	8.80
HFO-1234yf	2	257.39	3.900	16.54	6.00
n-$C_{10}H_{22}$	3	407.09	4.603	19.61	6.00
n-$C_{10}H_{22}$ (scaled)	3	414.90*	4.629*	19.61	6.00
n-$C_{20}H_{42}$	6	376.05	4.442	16.33	6.00
n-$C_{20}H_{42}$ (scaled)	6	398.51*	4.502*	16.33	6.00

[a]The five parameters are as follows: the number of segments per molecule m_s, the Mie potential well-depth ε (expressed in terms of the Boltzmann constant k_B), the diameter of the segments σ, and the repulsive and attractive Mie exponents, λ_r and λ_a. The Mie parameters are estimated from the experimental vapor−liquid equilibrium data using the SAFT-VR Mie EoS[66] as described in Section II.1; those indicated with the asterisk * are scaled using the procedure outlined in Section II.2.

II.2. Additional Scaling of the Model Parameters. As we will show in section IV, the SAFT-VR Mie EoS[66] is found to provide a high-fidelity description of the thermodynamic properties and fluid-phase equilibria of near-spherical molecules and dimers; in this case, the Helmholtz free energy of the fluid is described using a third-order Barker-Henderson[86] high-temperature perturbation expansion, using the Wertheim[54,56] TPT1 expression for the contribution due to the formation of the dimers in terms of the contact value of the pair distribution function of the reference monomer fluid. For large-chain molecules, the adequacy of the approximations inherent in the Wertheim TPT1 description of the chain contribution deteriorates as the chain length is increased; the issue is related to the use of the so-called linear approximation for the many-body distribution function of the monomer reference fluid which needs to be determined with high accuracy over the entire range of thermodynamic conditions of the fluid.[87] As a result, the SAFT description does not always provide the desired accuracy in representing the "exact" numerical thermodynamic properties obtained from molecular simulation for the longer chains. One could simply scale the size and energy parameters to the "exact" values for a single state point; for example, the critical point is often used for this purpose in engineering applications. In order to enhance the quality of the description, we instead perform a simple single-stage scaling procedure based on a comparison with a limited set of simulation data; specific details of the simulations will be given in the following section. This more formal procedure involves a consideration of the Helmholtz free-energy function $A^{sim}(m_s,\sigma,\varepsilon,\lambda_r,\lambda_a;\ N,V,T)$ of the model under investigation for a given set of molecular parameters which would correspond to the perfect representation of the simulated values at a specific thermodynamic state (i.e., with no approximations in the theory). We then assume that there exists a set of correction coefficients $(c_\sigma,c_\varepsilon,c_{\lambda_r},c_{\lambda_a})$ which satisfy the following relation for all canonical state points (NVT) in the fluid domain:

$$A^{sim}(m_s,\ \sigma,\ \varepsilon,\ \lambda_r,\ \lambda_a;\ N,\ V,\ T) = A^{SAFT}(m_s,\ c_\sigma\sigma,\ c_\varepsilon\varepsilon,\ c_{\lambda_r}\lambda_r,\ c_{\lambda_a}\lambda_a;\ N,\ V,\ T) \quad (4)$$

where A^{SAFT} is the Helmholtz free energy as described with the SAFT-VR Mie EoS. The scaling procedure then consists in determining the set of correction coefficients $(c_\sigma,c_\varepsilon,c_{\lambda_r},c_{\lambda_a})$ which would allow for a faithful representation of the simulated data. Moreover, if one assumes that the repulsive and attractive exponents λ_r and λ_a obtained during the original parameter estimation (cf. Section II.1) are reliable, then $c_{\lambda_r}=1$ and $c_{\lambda_a}=1$. This corresponds to the assumption of conformal behavior of the fluid models whereby the variable range of the Mie potential is adequately captured by the theory in the first iteration. The scaling of the intermolecular parameters therefore simply involves the use of the principle of corresponding states to determine the size and energy correction parameters c_σ and c_ε. Let σ^{SAFT} and ε^{SAFT} correspond to the original parameters estimated with the theory from the experimental data using eq 3. In principle, the scaling parameters c_σ and c_ε can be determined from the solution of eq 4 which formally relates the Helmholtz free energy as approximated with the SAFT-VR Mie EoS to the "exact" Helmholtz free energy. In practice, a strict equality cannot be enforced at all points, and we again employ a relative least-squares estimation based on the vapor pressure and saturated liquid density:

dx.doi.org/10.1021/jp306442b | J. Phys. Chem. B 2013, 117, 2717−2733

$$\min_{c_\sigma, c_\varepsilon} F_{\mathrm{obj,sim}}(c_\sigma, c_\varepsilon) = \min_{c_\sigma, c_\varepsilon} \left\{ \sum_{i=1}^{N_\mathrm{p}^\mathrm{sim}} \left[\left(P_\mathrm{v}^\mathrm{SAFT}(T_i; c_\sigma, c_\varepsilon; \sigma^\mathrm{SAFT}, \varepsilon^\mathrm{SAFT}, \lambda_\mathrm{r}, \lambda_\mathrm{a}, m_\mathrm{s}) - P_\mathrm{v}^\mathrm{sim}(T_i; \sigma^\mathrm{SAFT}, \varepsilon^\mathrm{SAFT}, \lambda_\mathrm{r}, \lambda_\mathrm{a}, m_\mathrm{s}) \right) / \left(P_\mathrm{v}^\mathrm{sim}(T_i; \sigma^\mathrm{SAFT}, \varepsilon^\mathrm{SAFT}, \lambda_\mathrm{r}, \lambda_\mathrm{a}, m_\mathrm{s}) \right) \right]^2 + \sum_{j=1}^{N_\rho^\mathrm{sim}} \left[\left({\rho_\mathrm{l}}^\mathrm{SAFT}(T_j; c_\sigma, c_\varepsilon; \sigma^\mathrm{SAFT}, \varepsilon^\mathrm{SAFT}, \lambda_\mathrm{r}, \lambda_\mathrm{a}, m_\mathrm{s}) - {\rho_\mathrm{l}}^\mathrm{sim}(T_j; \sigma^\mathrm{SAFT}, \varepsilon^\mathrm{SAFT}, \lambda_\mathrm{r}, \lambda_\mathrm{a}, m_\mathrm{s}) \right) / \left({\rho_\mathrm{l}}^\mathrm{sim}(T_j; \sigma^\mathrm{SAFT}, \varepsilon^\mathrm{SAFT}, \lambda_\mathrm{r}, \lambda_\mathrm{a}, m_\mathrm{s}) \right) \right]^2 \right\} \quad (5)$$

where $N_\mathrm{p}^\mathrm{sim}$ and N_ρ^sim represent the number of simulated values for the vapor pressure and saturated density, respectively, using the set of parameters labeled SAFT obtained from the original estimation step. Having determined the correction constants c_σ and c_ε, the scaled molecular parameters σ^sim and ε^sim recommended for use in molecular simulation are then simply obtained as $\sigma^\mathrm{sim} = \sigma^\mathrm{SAFT}/c_\sigma$ and $\varepsilon^\mathrm{sim} = \varepsilon^\mathrm{SAFT}/c_\varepsilon$. It is important to emphasize that the scaling scheme does not require an iterative molecular simulation procedure as the exponents λ_r and λ_a are not changed from the values obtained after the first stage of the parameter estimation. A schematic of the scaling procedure is given in the flowchart shown in Figure 1. As we will show in section IV, the single-segment and two-segment SAFT-γ CG Mie models developed here for CF_4, SF_6, CO_2, and HFO-1234yf provide an excellent description of the macroscopic fluid properties without the need for further adjustment. A scaling scheme is advantageous for large or more complex molecules, such as the long alkanes, n-$C_{10}H_{22}$ and n-$C_{20}H_{42}$, which are described with models comprising more than two CG segments. The procedure described in this section is used to obtain scaled parameters for the SAFT-γ CG Mie force fields of n-$C_{10}H_{22}$ and n-$C_{20}H_{42}$. The original and scaled parameters are collected in Table 1.

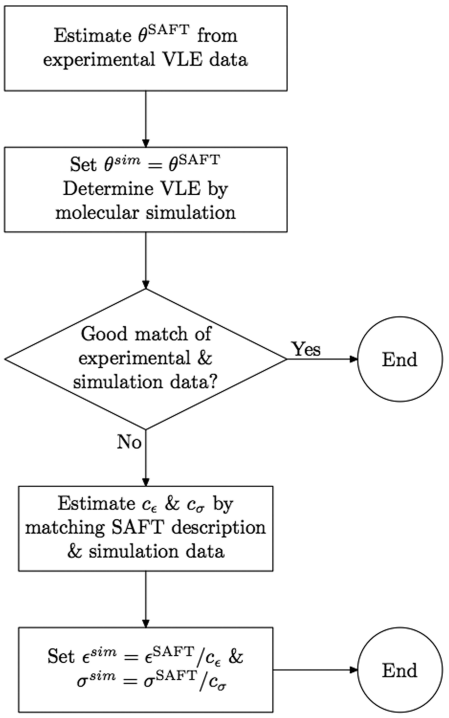

Figure 1. Flowchart of the procedure for the estimation of the SAFT-γ Mie intermolecular parameters θ^{SAFT} from the experimental vapor−liquid equilibria (VLE) data (vapor pressure and saturated liquid density). The vector of parameters θ^{SAFT} includes the number of Mie segments m_s making up the molecule, the segment diameter σ, the well depth ε, and the repulsive λ_r and attractive λ_a exponents; note that in our current study the number of segments is fixed *a priori*, and the London value of $\lambda_a = 6$ is assumed (with the exception of the CO_2 and SF_6 molecules where λ_a is also optimized). The single-step scaling procedure can be used to improve the description in cases where the SAFT calculations do not lead to models of the desired accuracy; c_σ and c_ε are the corresponding scaling parameters for the size and well depth of the Mie interaction for use in molecular simulation.

III. MOLECULAR SIMULATION METHODOLOGY

The systems are simulated using a molecular dynamics (MD) scheme. The Nosé-Hoover[88,89] thermostat with a relaxation constant of 0.2 ps is used to keep the temperature fixed, and the bond constraints are handled using the SHAKE algorithm;[90] all of the segment−segment bond lengths are kept fixed in this way, and the chain molecules are assumed to be completely flexible without allowing for segment overlaps. The equations of motion are solved using the leapfrog algorithm[14] with a time step of 1 fs, making use of the *DL_POLY2* software.[91] A potential cutoff of six times the diameter of the segment is used in all of the MD simulations; the potentials are not shifted, and standard long-range corrections are used. It has been shown by Trokhymchuk and Alejandre[92] that a cutoff of six diameters provides a reliable description for the pressure and interfacial properties of the Lennard-Jones fluid. We have checked that this choice of truncation is also adequate for our Mie potentials by comparison with the data for systems characterized by longer cutoffs and with the corresponding data obtained from Monte Carlo simulation with a long-range correction for the energy. In order to determine the fluid-phase equilibria, the vapor−liquid interface is explicitly included in the MD simulations.[93−95] This direct MD methodology has been shown to provide an essentially equivalent description of the coexistence properties obtained with other common methods such as Gibbs ensemble Monte Carlo (GEMC); there have however been recent reports of minor differences,[96] and we plan to make a detailed analysis of the fluid-phase equilibria obtained with the two techniques in future work. Direct MD offers a particular advantage when low-temperature states are considered, conditions where grand canonical μVT or GEMC simulation become highly inefficient due the low probability of insertion of particles at high density.[92,95,97−99] In our molecular simulations, the molecules are arranged in orthorhombic boxes of constant volume $V = L_x \times L_y \times L_z$ (L_i being the Cartesian box lengths) with standard periodic boundary conditions.[14,15] The overall density of the system is chosen such that the thermodynamic state lays inside the two-phase region to facilitate the formation of a vapor−liquid interface. The simulations are then performed in the canonical NVT ensemble, where the number of particles, the system volume, and the temperature are kept fixed. If the box dimensions are chosen such that $L_x = L_y = L \ll L_z$, where in our simulations the z-dimension is taken to be approximately three times larger

dx.doi.org/10.1021/jp306442b | J. Phys. Chem. B 2013, 117, 2717−2733

than the x and y dimensions, the system will eventually form a liquid slab with two planar interfaces along the z-direction so as to minimize the interfacial area. After the system reaches equilibrium, the properties of the coexisting vapor and liquid phases can be obtained as appropriate averages.

The vapor pressure P_v and vapor−liquid interfacial tension γ are obtained from the diagonal components of the pressure tensor $\mathbf{P}$. The vapor pressure corresponds to the normal component $P_v = P_{zz}$, while the surface tension is obtained from the difference of the averages of the normal and tangential components:[100−102]

$$\gamma = \frac{1}{2}L_z\left[P_{zz} - \frac{1}{2}(P_{xx} + P_{yy})\right] \quad (6)$$

where the leading prefactor of 1/2 denotes the presence of two interfaces. The coexistence densities are obtained directly from appropriate averages of the density profiles $\rho(z)$ in the corresponding bulk regions. The critical temperature T_c is obtained using a first-order Wegner expansion[103,104]

$$\rho_l - \rho_v = B_0|\tau|^{\beta_c} + B_1|\tau|^{\beta_c+\Delta} \quad (7)$$

where ρ_l and ρ_v are the number densities of the coexisting liquid and vapor phases, respectively, $\tau = 1 - T/T_c$ characterizes the departure from the critical temperature, $\beta_c = 0.325$ is the critical exponent which is fixed at its universal renormalization-group value, $\Delta = 0.51$ is the so-called gap-exponent, and B_i are the correction amplitudes obtained by correlating the simulation data.[104] Once the critical temperature is determined, the critical density ρ_c and critical pressure P_c are obtained using the law of rectilinear diameters and the Clausius−Clapeyron relation

$$\frac{\rho_l + \rho_v}{2} = \rho_c + D|\tau| \quad (8)$$

and

$$\ln P = E + F/T \quad (9)$$

where D, E, and F are correlation parameters (the latter two relating to the entropy and enthalpy of vaporization).

Second derivative thermodynamic properties are obtained by Monte Carlo simulation in the isothermal−isobaric NPT ensemble, based on an analysis of averages of the fluctuations in the configurational internal energy, the configurational enthalpy, and the volume. A potential cutoff of four times the diameter of the segment is used, with a standard long-range correction for the energy; the truncation of the potential and the use of long-range corrections for the configurational energy is not problematic for reasonably large cutoffs such as the one used here, giving essentially identical results to those for systems with a larger value of the cutoff. For precise details of the MC methodology, the reader is directed to our first article of this series[47] and to refs 105−107.

IV. RESULTS

IV.1. Single-Segment Coarse-Grained Mie Models. We start by developing spherically symmetrical SAFT-γ CG Mie force fields for carbon tetrafluoride and sulfur hexafluoride. The grand canonical Monte Carlo results for a single-segment SAFT-γ model of carbon dioxide presented in a previous paper[47] are complemented with new molecular dynamics simulation data obtained in our current work. These molecular fluids provide good examples of the versatility of simple CG Mie potentials in accurately describing the fluid-phase equilibria and thermodynamic properties of small molecules with challenging intermolecular potentials, by making use of appropriate choices of the repulsive and attractive exponents. The SAFT-γ CG Mie parameters for CO_2, CF_4, and SF_6 estimated from the experimental vapor-pressure and saturated liquid density data with the SAFT-VR Mie EOS are reported in Table 1; in this case, no additional scaling of the parameters is necessary. It is interesting to note that values obtained for the attractive exponent of CO_2 and SF_6 are larger than the London dispersion value of $\lambda_a = 6$; this is consistent with the higher multipole moments that are active in these compounds, though the description of these nonspherical molecules as spherical CG models may also be responsible for a departure from the London value.

In order to quantify the quality of the description of the thermodynamic properties obtained with our CG models by molecular simulation, we compute the percentage average absolute deviation AAD% with respect to the experimental data

$$\mathrm{AAD\%} = \frac{1}{N_p}\sum_{i=1}^{N_p}\left|\frac{X_i^{exp} - X_i^{sim}}{X_i^{exp}}\right| \times 100 \quad (10)$$

where X_i^{exp} and X_i^{sim} are the experimental and simulated properties, respectively. The MD data obtained for the fluid-phase coexistence using the SAFT-γ CG Mie force fields for CO_2, CF_4, and SF_6 are presented in Figures 2−5. The simulated values are compared with the available experimental data,[85] with the theoretical description obtained using the SAFT-VR Mie EoS[66] (cf. the Appendix), and with the simulation data for a LJ model using molecular parameters that reproduce the experimental critical temperature and density using the principle of corresponding states[108,109] (the benchmark VLE data for the LJ fluid are taken from refs 110 and 111, while the

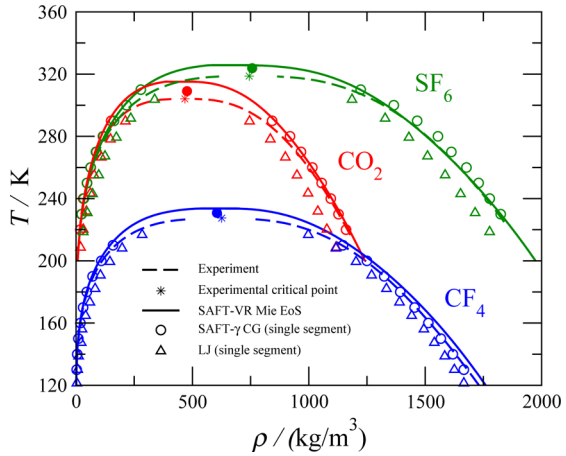

Figure 2. Temperature−density vapor−liquid coexistence envelopes for carbon dioxide (CO_2), carbon tetrafluoride (CF_4), and sulfur hexafluoride (SF_6). The dashed curves denote the smoothed experimental data from NIST,[85] the continuous curves the description obtained with the SAFT-VR Mie EoS,[66] the circles are the results obtained by molecular dynamics simulation using the single-segment SAFT-γ CG Mie models for the three different molecules, and the triangles represent the description with the Lennard-Jones potential using molecular parameters that reproduce the experimental critical temperatures and densities. The asterisks represent the experimental critical points, and the filled circles the critical points estimated from the simulation data for the corresponding SAFT-γ CG Mie models.

dx.doi.org/10.1021/jp306442b | J. Phys. Chem. B 2013, 117, 2717−2733

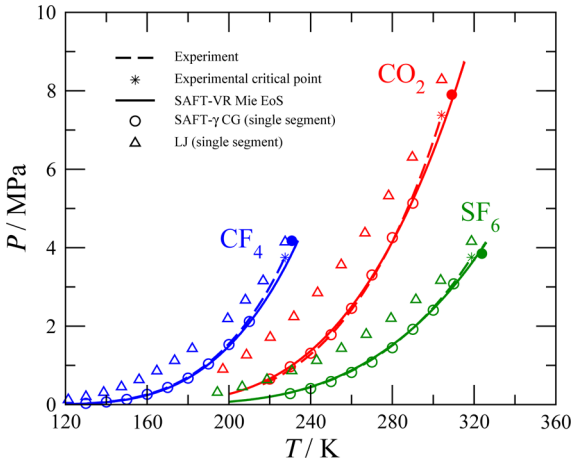

Figure 3. Vapor pressure as a function of temperature for carbon dioxide (CO_2), carbon tetrafluoride (CF_4), and sulfur hexafluoride (SF_6). Legend as in Figure 2.

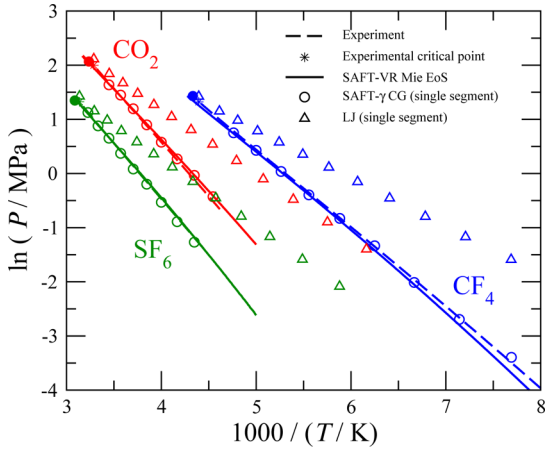

Figure 4. Vapor pressure in the Clausius−Clapeyron representation for carbon dioxide (CO_2), carbon tetrafluoride (CF_4), and sulfur hexafluoride (SF_6). Legend as in Figure 2.

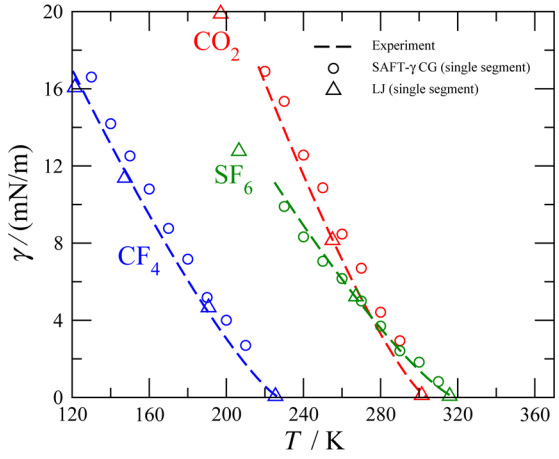

Figure 5. Vapor−liquid interfacial tension as a function of temperature for carbon dioxide (CO_2), carbon tetrafluoride (CF_4), and sulfur hexafluoride (SF_6). Legend as in Figure 2, with the exception of the theoretical curves as the macroscopic SAFT-VR EoS does not provide a direct description of the interfacial properties.

critical temperature is taken as $T_c^* = k_B T_c/\varepsilon = 1.312$ and the critical density as $\rho_c^* = \rho_c\sigma^3 = 0.316$ according to ref 112). As can be observed from Figure 2 the densities of the coexisting vapor and liquid phases obtained using our single-segment SAFT-γ CG models for CO_2, CF_4, and SF_6 are in good agreement with the experimental data. The overall AADs% for the saturated liquid density are 1.7% for CO_2 over the temperature range 220−290 K, 0.5% for CF_4 over the range 130−210 K, and 2.1% for SF_6 over the range 230−300 K. It is also apparent that though the description of the coexistence densities with the LJ model is reasonable, it is clearly less accurate than with the CG models based on the Mie potential, particularly in the case of CO_2; the corresponding AADs% for the saturated liquid density obtained with the LJ models are 7.2% for CO_2, 3.5% for CF_4, and 5.7% for SF_6.

The single-segment SAFT-γ models provide a good description of the vapor pressure for CO_2, CF_4, and SF_6. The results are presented in Figure 3 where it is apparent that the representation with our force fields is in good agreement with the experimental data. The description of the vapor pressure with the SAFT-γ Mie force fields at low temperatures (cf. the Clausius−Clapeyron representation shown in Figure 4) is remarkable considering that these are simple CG single-segment models. The AADs% obtained for the vapor pressure over the same temperature ranges as the saturated liquid density are 3.7% for CO_2, 3.6% for CF_4, and 5.3% for SF_6. The vapor pressure obtained with the LJ 12−6 potential is also presented in Figures 3 and 4. One should again note that the LJ parameters are determined by matching only the experimental critical temperature and density. The AADs% for the vapor pressure obtained with the LJ potential are 84.3% for CO_2, 190.0% for CF_4, and 80.3% for SF_6. The CG LJ force fields are seen to be inadequate for this property; an improvement could be achieved by using the critical pressure rather than the critical density to obtain the parameters; this would of course lead to a deterioration in the representation of the coexistence densities, and the slope of vapor-pressure curve (Clausius−Clapeyron representation) would still be poorly represented. In general, the simulation results for SAFT-γ Mie models are in very good agreement with experiments. It is gratifying to see that for these near-spherical molecules high-fidelity force-field parameters can be obtained directly from macroscopic data using the SAFT-VR Mie EoS without the need for scaling.

The critical properties obtained for our SAFT-γ CG Mie models of CO_2, CF_4, and SF_6 are reported in Table 2. It is well-known that equation-of-state approaches fail in the critical region unless an appropriate renormalization treatment is made; though such a procedure can be implemented within a SAFT formalism (e.g., see refs 113−118), this is beyond the scope of the current paper. During the parameter estimation, only vapor−liquid coexistence data at low to moderate temperatures, i.e., well below the critical temperature, are used. For this reason, the inadequate treatment of the critical region with the EoS is not reflected in the prediction of the critical properties obtained from the molecular simulation data with the Wegner extending scaling relations. Nonetheless, small deviations of the predicted critical properties are observed when compared with the experimental values: for CO_2, CF_4, and SF_6, these deviations are found to be less than 1.6% for the critical temperature and less than 3.2% for the critical density, though the deviation of the critical pressures can be as much as 11% in the case of CF_4.

dx.doi.org/10.1021/jp306442b | J. Phys. Chem. B 2013, 117, 2717−2733

Table 2. Experimental and Predicted Critical Properties for the Systems Studied[a]

	experimental			SAFT-γ CG Mie		
molecule	T_c/K	ρ_c/(kg/m^3)	P_c/MPa	T_c/K	ρ_c/(kg/m^3)	P_c/MPa
CO_2	304.13	467.60	7.3773	309.05	476.93	7.9016
CF_4	227.51	625.66	3.7500	230.81	605.15	4.1769
SF_6	318.73	743.81	3.7546	323.82	756.75	3.8495
HFO-1234yf	367.85	478.00	3.3820	367.90	467.64	3.4891
n-$C_{10}H_{22}$	617.70	233.00	2.1030	611.53	230.54	3.2153
n-$C_{10}H_{22}$(scaled)				620.77*	227.67*	2.7922*
n-$C_{20}H_{42}$	768.00	241.58	1.1746	748.56	221.81	1.5206
n-$C_{20}H_{42}$(scaled)				793.26*	213.09*	1.5481*

[a]The experimental values for CO_2, CF_4, SF_6, and n-$C_{10}H_{22}$ are taken from ref 85, the values for HFO-1234yf are taken from ref 123, and the values for n-$C_{20}H_{42}$ are taken from ref 127. The critical properties are calculated from the simulated data for the SAFT-γ CG Mie force fields with the Wegner extended scaling relations (cf. Section III); the values obtained for the models with parameters estimated from the experimental VLE data using the SAFT-VR Mie EoS[66] are shown, together with those for the scaled models, indicated with the asterisk *.

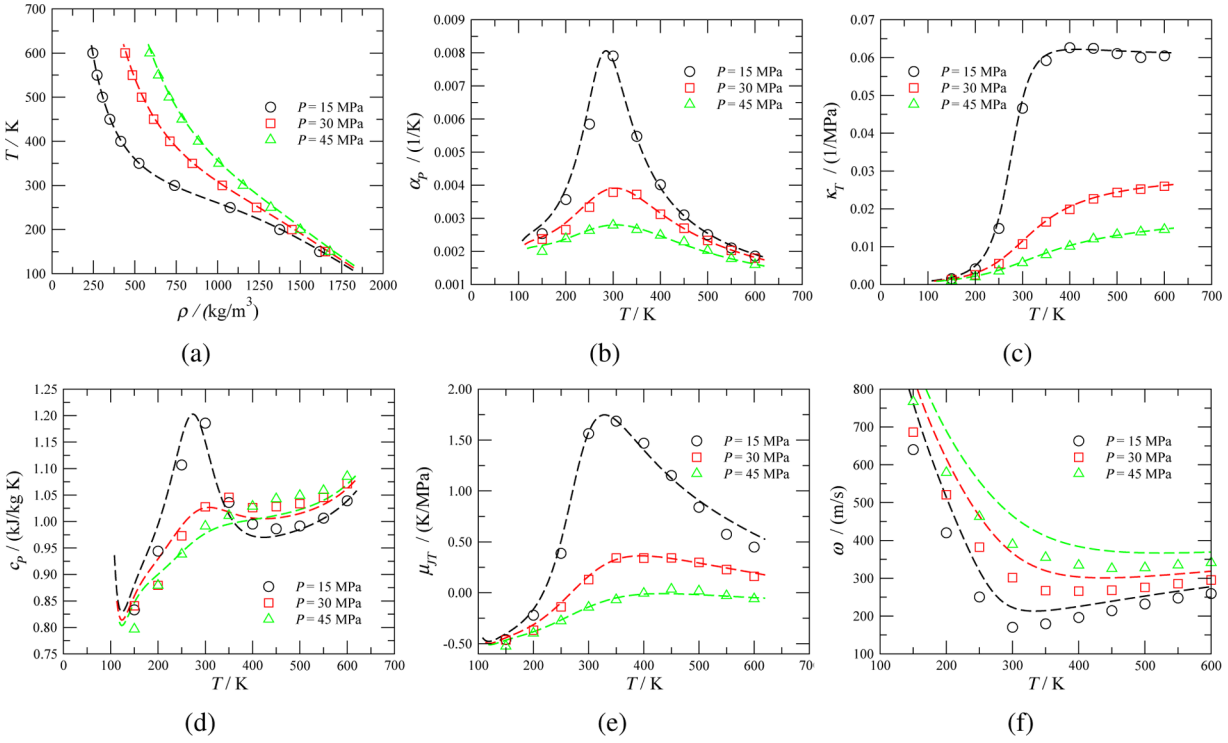

Figure 6. Temperature and pressure dependence of (a) the density ρ, (b) the coefficient of thermal expansion $\alpha_P = (1/V)(\partial V/\partial T)_P$, (c) the isothermal compressibility $\kappa_T = -(1/V)(\partial V/\partial P)_T$, (d) the isobaric heat capacity $c_P = (\partial h/\partial T)_P$, (e) the Joule-Thomson coefficient $\mu_{JT} = (\partial T/\partial P)_P$, and (f) the speed of sound ω for carbon tetrafluoride (CF_4). The dashed curves denote the smoothed experimental data from NIST,[85] and the symbols are the results obtained by Monte Carlo simulation with the single segment SAFT-γ CG Mie model.

We reiterate here that the intermolecular force fields are obtained by parameter estimation with the SAFT-VR EoS using experimental data for the saturated liquid density and vapor pressure. A good test of the SAFT-γ Mie models is the simulation of properties not employed in the estimation procedure. In our current work, we exemplify the predictive capability of the models by determining the interfacial tension and second derivative thermodynamic properties. The vapor–liquid interfacial tension obtained by MD simulation of the SAFT-γ CG models for the three systems are compared with the corresponding experimental data[85] in Figure 5. In the case of CO_2 and CF_4, the intermolecular potentials predict the correct temperature dependence of the interfacial tension, but the values are slightly overestimated by an almost constant amount of about 1 mN/m. For SF_6, the simulations underpredict the experimental data at low temperatures and then overpredict the interfacial tension for the higher temperature states. As in the case of CO_2, the cause of the deviations is mainly the slight overprediction of the critical temperature with the SAFT-γ CG Mie models; a simple scaling of the well-depth parameter ε to the critical temperature can be used to improve the description of the interfacial tension.[47]

We have already shown[47] that the SAFT-γ CG Mie model for CO_2 provides a very good description of volumetric and second derivative properties. Here, a similar analysis is made for the SAFT-γ CG Mie models of CF_4 and SF_6. The predictions for the coefficient of thermal expansion, isothermal compressibility, isobaric heat capacity, Joule-Thomson coefficient, and speed of sound (together with values of the bulk liquid density) obtained from *NPT* MC simulations (cf. ref 47) for three supercritical

dx.doi.org/10.1021/jp306442b | J. Phys. Chem. B 2013, 117, 2717–2733

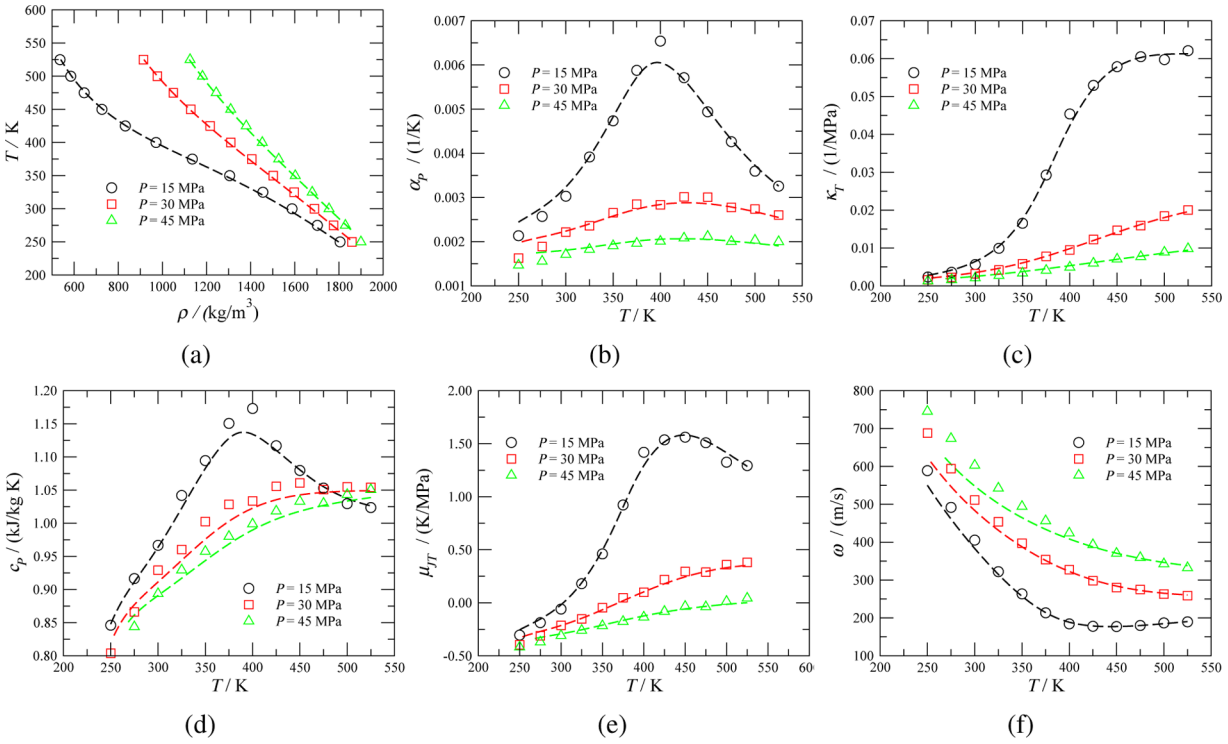

Figure 7. Temperature and pressure dependence of (a) the density ρ, (b) the coefficient of thermal expansion $\alpha_P = (1/V)(\partial V/\partial T)_P$, (c) the isothermal compressibility $\kappa_T = -(1/V)(\partial V/\partial P)_T$, (d) the isobaric heat capacity $c_P = (\partial h/\partial T)_P$, (e) the Joule-Thomson coefficient $\mu_{JT} = (\partial T/\partial P)_P$, and (f) the speed of sound ω for sulfur hexafluoride (SF_6). The dashed curves denote the smoothed experimental data from NIST,[85] and the symbols are the results obtained by Monte Carlo simulation with the single-segment SAFT-γ CG Mie model.

isobars, corresponding to P = 15, 30, and 45 MPa, are presented in Figures 6 and 7. The description of the volumetric and derivative properties with the SAFT-γ CG Mie force fields is generally found to be very good, particularly considering that these are predictions and that the models are simple. In the case of CF_4, the AADs% for these properties are: 0.9% for the density ρ, 2.9% for the coefficient of thermal expansion α_P, 5.7% for the isothermal compressibility κ_T, and 2.3% for the isobaric heat capacity c_p. A similar agreement is found for the volumetric and second derivative properties of SF_6, with corresponding AADs% of 0.6% for ρ, 3.5% for α_P, 6.2% for κ_T, and 1.2% for c_p. In the same figures, one can observe that the prediction of the Joule-Thomson coefficient μ_{JT} and the speed of sound ω is good compared with the experimental values, though the large relative deviations in these quantities lead to larger AADs% of ~15%, which is still acceptable considering that these are derivative properties. Despite this observation, our simple models capture the correct behavior of these properties.

IV.2. Two-Segment Coarse-Grained Mie Model. The novel refrigerant 2,3,3,3-tetrafluoro-1-propene (HFO-1234yf) has recently been of particular interest due to its promising properties.[77] To the best of our knowledge, the only reports of the fluid-phase behavior of HFO-1234yf by molecular simulation have involved force fields of the AMBER[119,120] and OPLS[121] forms. In our current paper, we develop a very simple SAFT-γ CG force field by representing the molecule as a homonuclear two-segment model comprising tangent Mie segments. The fluid-phase coexistence data simulated with our tangent dimer SAFT-γ CG Mie model are presented in Figures 8–11. The simulated values are also compared with the experimental data of Tanaka and Higashi,[122,123] and with the

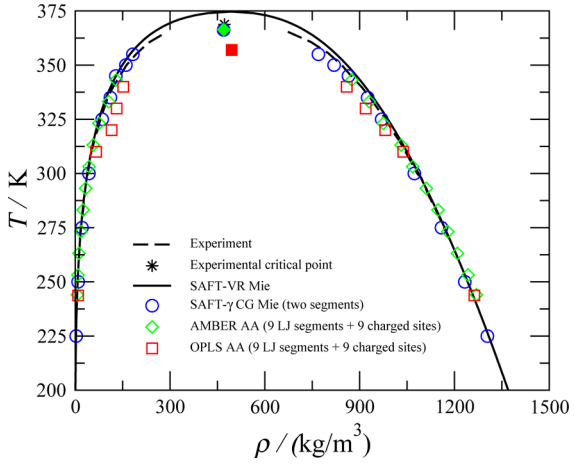

Figure 8. Temperature–density vapor–liquid coexistence envelope for 2,3,3,3-tetrafluoro-1-propene (HFO-1234yf). The dashed curve denotes the smoothed experimental data of Tanaka and Higashi,[122] the continuous curve is the description with the SAFT-VR Mie EoS,[66] the circles are the results obtained by molecular dynamics simulation using our two-segment tangent SAFT-γ CG Mie model, the diamonds are the results reported by Raabe and Maginn[119] using a model based on the all-atom AMBER force field, and the squares are those of Paulechka et al.[121] using a model based on the all-atom OPLS force field. The asterisk denotes the experimental critical point, and the filled symbols are the corresponding values estimated from the simulation data for the various models.

theoretical description with the SAFT-VR Mie EoS. In Figure 8, the densities of the coexisting phases are presented, where one can observe that the simulation data obtained with our model are in good agreement with the experimental data including the

dx.doi.org/10.1021/jp306442b | J. Phys. Chem. B 2013, 117, 2717–2733

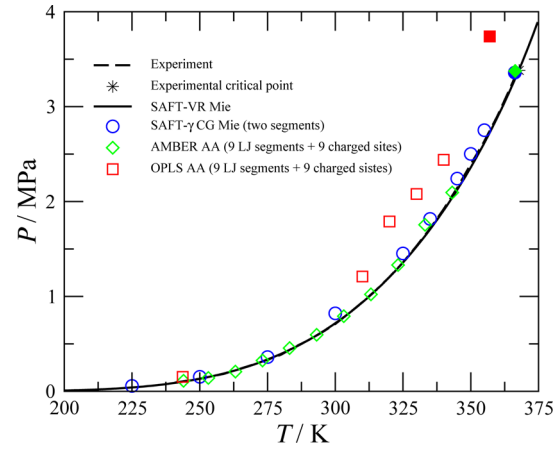

Figure 9. Vapor pressure as a function of temperature for 2,3,3,3-tetrafluoro-1-propene (HFO-1234yf). Legend as in Figure 8.

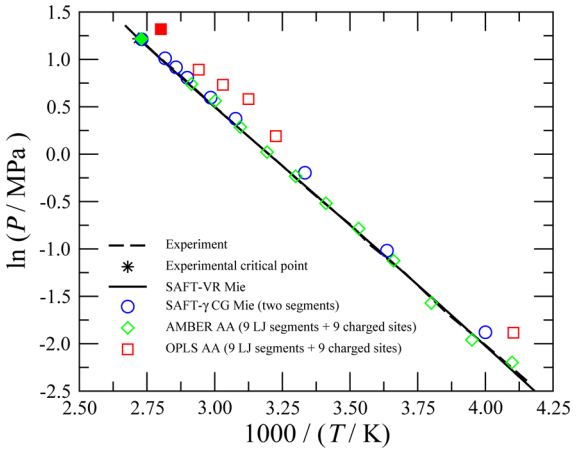

Figure 10. Vapor pressure in the Clausius–Clapeyron representation for 2,3,3,3-tetrafluoro-1-propene (HFO-1234yf). Legend as in Figure 8.

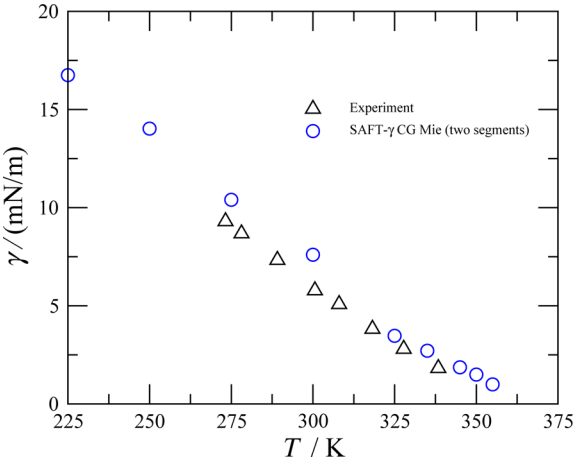

Figure 11. Vapor–liquid interfacial tension as a function of temperature for 2,3,3,3-tetrafluoro-1-propene (HFO-1234yf). The triangles represent the experimental data of Tanaka and Higashi,[123] and the circles are the results obtained by molecular dynamics simulation using our two-segment tangent SAFT-γ CG Mie model.

critical region; the results for the critical point of HFO-1234yf are summarized in Table 2. A good description of the vapor-pressure curve and its Clausius–Clapeyron representation can be achieved with the SAFT-γ CG Mie force field, though a small systematic overestimation of this property is apparent. However, considering the simplicity of the model for this complex polar molecule the description is very encouraging. The quality of the representation can be seen from average deviations with corresponding ADDs% of 1.4% for the saturated liquid density and 7.1% for the vapor pressure. For completeness, we compute the vapor–liquid interfacial tension for our tangent dimer SAFT-γ CG Mie model, and compare the simulated values with the experimental data.[123] The predicted values are shown in Figure 11, where good agreement is apparent, with only a small overestimation of the interfacial tension.

We also compare the representation of our model with the simulation data reported for more sophisticated all-atom force fields comprising nine LJ segments and 9 partial charges. Our simple two-segment SAFT-γ CG Mie model of HFO-1234yf is found to provide a description of similar quality to that obtained with the AMBER model of Raabe and Maginn,[119] and a very large improvement compared with the results reported by Paulechka et al.[121] with their OPLS model. A key advantage of representing the fluid-phase equilibria of this system with our simple two-segment model is the very significant reduction in the number of interaction sites that need to be considered with the AA models (nine LJ segments plus 9 partial charges); one also avoids the need for special methods to deal with electrostatic interactions, such as the Ewald, reaction-field, and Wolf techniques which are computationally very expensive.[14,124,125] By using our CG models, a savings of almost 2 orders of magnitude in computing time can be achieved for this system.

IV.3. Chains of Coarse-Grained Mie Segments. Even when an adequate description of the softness/hardness of the repulsions and the range of the attraction of the intermolecular potential can be achieved with a Mie force field, single-segment or dimer CG models will become increasingly inappropriate as the molecules become more elongated; the marked non-sphericity has to be accounted for explicitly. For long linear and branched alkanes, polymeric molecules, amphiphiles, etc., several segments each corresponding to the coarse-grained functional groups are required to adequately represent the chemical moieties. As prototypical examples, we examine hydrocarbon molecules represented as fully flexible chains of tangent spherical Mie segments. We have chosen to model *n*-decane and *n*-eicosane as tangent chains of $m_s = 3$ and $m_s = 6$ CG segments, respectively. The CG parameters for the segment–segment interactions estimated from the experimental vapor–liquid equilibrium data[85,126,127] using the SAFT-VR Mie EoS are reported in Table 1. We note that at this level of coarse graining the parameters characterizing the segments of the alkyl chains are different (cf. the values for *n*-decane and *n*-eicosane in Table 1); clearly, the terminal methyl groups will have a more marked effect on the thermodynamic properties of the shorter chains, which is reflected in the different values of the parameters for the CG segments. The lack of transferability in CG models is a well-known issue,[19,21−25] where the parameters are often found to be system (and state) dependent. Transferable CG models could be developed within our SAFT-γ methodology by simultaneously estimating the parameters from the vapour-liquid equilibria for a range of alkanes, but this would be at the expense of accuracy of description. Lower levels of coarse graining, such as, for example, a united-atom representation with explicit methyl and methylene groups,

dx.doi.org/10.1021/jp306442b | J. Phys. Chem. B 2013, 117, 2717−2733

would be required to ensure better transferability of the segment parameters.

The fluid-phase coexistence densities for both *n*-decane and *n*-eicosane obtained with our SAFT-γ CG Mie force fields by direct molecular dynamics simulation are shown in the inset of Figure 12. The simulation data are compared with the

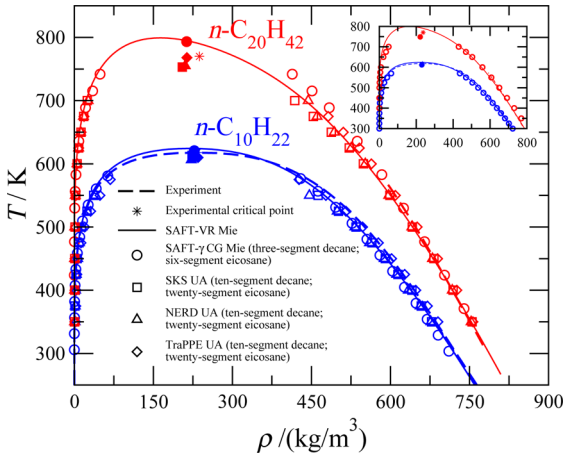

Figure 12. Temperature−density vapor−liquid coexistence envelopes for *n*-decane (*n*-$C_{10}H_{22}$) and *n*-eicosane (*n*-$C_{20}H_{42}$). The dashed curves denote the smoothed experimental data,[85,126,127] the continuous curves the description obtained with the SAFT-VR Mie EoS (using the original unscaled parameters), the circles are the results obtained by molecular dynamics simulation using the scaled SAFT-γ CG Mie fully flexible tangent chain models. The corresponding molecular simulation data for *n*-decane and *n*-eicosane using the SKS (squares),[129,130] NERD (triangles),[131] and TraPPE (diamonds)[74] united-atom (UA) force fields, taken from ref 128, are shown for comparison. The asterisks represent the experimental critical points, and the filled symbols are the critical values estimated from the simulation data for the various models. In the inset, we compare the corresponding description obtained with the unscaled SAFT-γ CG Mie models which are estimated directly from the experimental VLE data using the SAFT-VR Mie EoS alone.

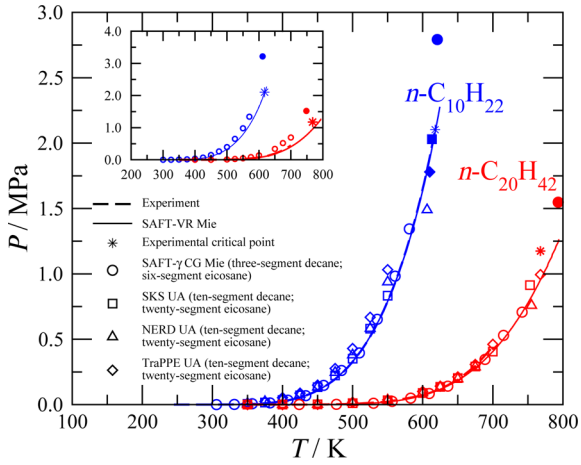

Figure 13. Vapor pressure as a function of temperature for *n*-decane (*n*-$C_{10}H_{22}$) and n-eicosane (*n*-$C_{20}H_{42}$). Legend as in Figure 12.

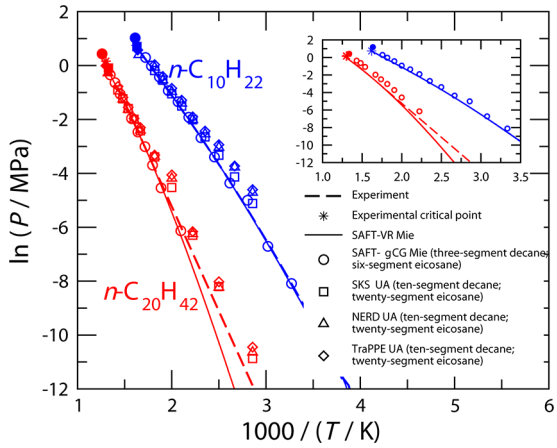

Figure 14. Vapor pressure in the Clausius−Clapeyron representation for *n*-decane (*n*-$C_{10}H_{22}$) and *n*-eicosane (*n*-$C_{20}H_{42}$). Legend as in Figure 12.

description from the SAFT-VR Mie EoS and with experimental data. The coexistence densities for both systems are seen to be in good agreement with the experimental values. The AAD% relative to the experimental data obtained for the saturated liquid density with the SAFT-γ CG force fields is 1.9% for both the three-segment model of *n*-decane over the temperature range 300−570 K and the six-segment model of *n*-eicosane over the temperature range 400−700 K. The simulated vapor pressures obtained for the SAFT-γ CG Mie chains are compared with the theoretical description and the experimental data in the inset of Figure 13. It is clear that the representation obtained with model parameters that are estimated directly using the theory without additional scaling is not as accurate as that found for the smaller molecules examined in Sections IV.1 and IV.2, with the corresponding AADs% for the vapor pressure now between 25% and 200%; the deterioration is particularly marked for *n*-eicosane at lower temperatures (as is apparent from the Clausius−Clapeyron representation shown in the inset of Figure 14), though one should recognize that the absolute values of the pressure are very small for long-chain molecules in this region. In order to improve the description of the vapor pressure for these chain molecules, we employ the procedure described in Section II.2; the scaled parameters for the SAFT-γ CG Mie models of *n*-decane and *n*-eicosane are also included in Table 1. As can be seen in the main body of Figures 13 and 14, these scaled parameters lead to a significant improvement in the representation of the vapor-pressure curve for *n*-decane and more particularly for *n*-eicosane (cf. the insets of Figures 13 and 14), with an essentially equivalent description of the coexistence densities (cf. Figure 12 and its inset). The ADDs% for the saturated liquid density of the scaled model are 1.9% for *n*-decane and 0.7% for *n*-eicosane, while much improved ADDs% of 5.3% for *n*-decane and 29.3% for *n*-eicosane are found for the vapor pressure.

The adequacy of the description of the simulated vapor−liquid equilibria of *n*-decane and *n*-eicosane obtained with our SAFT-γ CG Mie models is also compared with existing simulation data[128] for the commonly employed united-atom intermolecular potentials for alkanes such as the SKS,[129,130] NERD,[131] and TraPPE[74] force fields. Although the saturated liquid density is found to be described to a similar level of accuracy with the various force fields, the representation of the vapor pressure of *n*-decane and *n*-eicosane obtained with our CG models is superior. In the case of *n*-decane, the AAD% relative to the experimental vapor pressure for the three-segment SAFT-γ CG Mie model is 5.3%, compared to 16.6% for the SKS, 39.1% for the NERD, and 53.9% for the TraPPE models over the same temperature range. For *n*-eicosane, the

dx.doi.org/10.1021/jp306442b | J. Phys. Chem. B 2013, 117, 2717−2733

corresponding AAD% for the six-segment SAFT-γ CG Mie model is 29.3%, compared to 50.8% for the SKS, 70.6% for the NERD, and 76.6% for the TraPPE models.[128]

The values of the interfacial tension predicted from direct MD simulation of the vapor−fluid interfaces of the SAFT-γ CG Mie chain models for *n*-decane and *n*-eicosane are compared with the corresponding experimental data[85,127] in Figure 15.

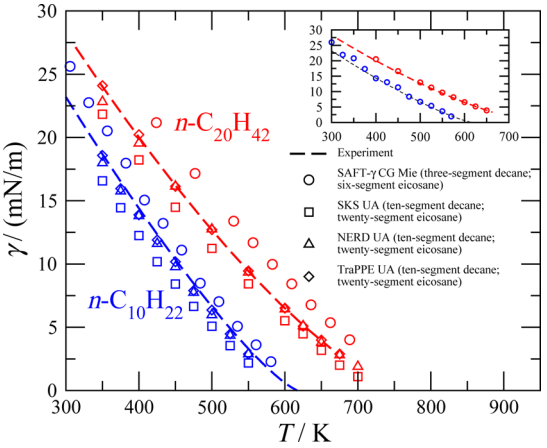

Figure 15. Vapor−liquid interfacial tension as a function of temperature for *n*-decane (n-$C_{10}H_{22}$) and *n*-eicosane (n-$C_{20}H_{42}$). Legend as in Figure 12.

The description obtained for the interfacial tension with force-field parameters estimated from the experimental saturated liquid density and vapor pressure data without additional scaling are found to be in very good agreement with experiment (cf. the inset of Figure 15); it is pleasing to see that for *n*-decane the overestimate of the critical temperature does not appear to affect the accuracy of the description of the interfacial tension. This provides a good indication of the transferability of the models to properties that are not used in the estimation of the force-field parameters. Although the scaled SAFT-γ parameters for *n*-eicosane lead to a much better description of the vapor-pressure curve, the refinement results in a slight overestimation in the predicted value of the critical temperature, which leads to a corresponding small shift of the surface tension curve by about ∼2 mN/m (cf. the main body of Figure 15).

V. CONCLUSIONS

Novel coarse-grained SAFT-γ force fields based on the Mie potential for carbon tetrafluoride, sulfur hexafluoride, the refrigerant 2,3,3,3-tetrafluoro-1-propene, and the long-chain hydrocarbons *n*-decane and *n*-eicosane are developed, using the SAFT-VR Mie EoS to estimate the parameters of the Mie interaction from macroscopic fluid-phase equilibrium data. As for carbon dioxide, which was the focus of a previous study,[47] simple single-segment coarse-grained models are used to represent carbon tetrafluoride and sulfur hexafluoride, while a two-segment homonuclear model is used to represent 2,3,3,3-tetrafluoro-1-propene. A representation of the thermodynamic and phase equilibrium properties of these systems is challenging due to the high polarizability of perfluorinated compounds (e.g., the value for SF_6 is more than twice that of methane), giving rise to unusual features in the balance of the repulsive and attractive contributions to the intermolecular potential which cannot be captured with a simple Lennard-Jones potential. The versatility of the Mie (generalized Lennard-Jones) form in controlling the softness/hardness and range of the potential is a particular strength of the SAFT-γ force fields. In the case of carbon tetrafluoride, sulfur hexafluoride, and 2,3,3,3-tetrafluoro-1-propene, the SAFT-γ CG Mie force field parameters estimated from experimental data using the SAFT-VR Mie EoS[66] provide an excellent description of the vapor−liquid equilibria without the need for further adjustment. Predictions of the vapor−liquid interfacial tension and second derivative thermodynamic properties (such as the coefficient of thermal expansion, isothermal compressibility, isobaric heat capacity, Joule-Thomson coefficient, and speed of sound), which are not considered in the parameter estimation procedure, are also represented well with our simple CG models. The long alkanes are modelled as fully flexible homonuclear chains formed from a number of tangentially bonded CG Mie segments: in this instance three segments are used to represent *n*-decane and six to represent *n*-eicosane. The description obtained for the vapor−liquid equilibria (saturated liquid density and vapor pressure) with the SAFT-γ CG Mie force field is of comparable accuracy to that obtained with the more sophisticated SKS, NERD, and TraPPE united-atom models: the coexisting densities are accurately represented, but the deviation of the vapor pressure is relatively large (with an AAD% relative to experimental data of between 25% to 200%). In order to provide an improved representation of the vapor pressure of the system, the model parameters estimated from the experimental data with the SAFT-VR Mie EoS are scaled by using the simulation data within a simple scheme. This then allows the vapor pressure of *n*-decane to be described with an ADD% relative to the experimental data of less than 6% without a significant deterioration in the representation of the saturated liquid density. In contrast to traditional approaches for the development of intermolecular potential models with a trial-and-error procedure involving multiple simulations (computations that can take weeks or months), the SAFT-γ force fields are parametrized using an analytical closed-form equation of state, which is far less computationally demanding (typically involving only a few seconds). We are continuing to expand the SAFT-γ CG Mie parameter database to include other compounds and to develop heteronuclear models in which CG groups of different type are used to represent molecules comprising chemical goups of varying functionality (e.g., *n*-decyl benzene[132]). The SAFT-γ EoS,[67−69] which is at the heart of our methodology, is cast as a group contribution approach which is appropriate for molecules formed from chemical groups of different type and can thus be used to parameterize heteronuclear models in a straightforward manner. The methodology is currently being employed to develop CG force fields for use in the simulation of aqueous solutions of amphiphilic molecules (ionic and nonionic surfactants) and polymeric systems.

■ APPENDIX

We summarize the principal relations of the SAFT-VR Mie equation of state used in our current work to develop the SAFT-γ CG Mie force fields for the single-segment model of CF_4, SF_6, and CO_2, the two-segment model of HFO-1234yf, the three-segment model of n-$C_{10}H_{22}$, and the six-segment model of n-$C_{20}H_{42}$. The formal development of the thermodynamic perturbation theory for chains of Mie segments can be found in ref 66. We should point out that there were a few typographical errors in the expressions reported in the

dx.doi.org/10.1021/jp306442b | J. Phys. Chem. B 2013, 117, 2717−2733

Table 3. Coefficients $\phi_{i,n}$ for eq 29 and eq 40

n	$\phi_{1,n}$	$\phi_{2,n}$	$\phi_{3,n}$	$\phi_{4,n}$	$\phi_{5,n}$	$\phi_{6,n}$	$\phi_{7,n}$
0	7.5365557	−359.44	1550.9	−1.19932	−1911.28	9236.9	10
1	−37.60463	1825.6	−5070.1	9.063632	21390.175	−129430	10
2	71.745953	−3168.0	6534.6	−17.9482	−51320.7	357230	0.57
3	−46.83552	1884.2	−3288.7	11.34027	37064.54	−315530	−6.7
4	−2.467982	−0.82376	−2.7171	20.52142	1103.742	1390.2	−8
5	−0.50272	−3.1935	2.0883	−56.6377	−3264.61	−4518.2	-
6	8.0956883	3.7090	0	40.53683	2556.181	4241.6	-

appendix of ref 47 which are rectified here for clarity [cf. eqs 23, 24, 26, 28, 32, 39, and Table 3]; theses errors did not affect any of the calculations reported in ref 47.

The general formulation of the (dimensionless) Helmholtz free energy for a nonassociating chain fluid is expressed in the usual SAFT manner as

$$a = a^{IDEAL} + a^{MONO} + a^{CHAIN} \tag{11}$$

where $a = A/(Nk_BT)$, A being the total Helmholtz free energy, N the total number of molecules, V the volume of the system, T the temperature, and k_B the Boltzmann constant. In eq 11, a^{IDEAL} is the contribution of the ideal free energy, a^{MONO} is the residual free energy corresponding to the monomeric segments, and a^{CHAIN} is the contribution due to the formation of chains of monomers.

A1. Ideal Contribution

The ideal gas contribution is given in the usual form as

$$a^{IDEAL} = \ln(\rho\Lambda^3) - 1 \tag{12}$$

where $\rho = N/V$ is the number density of chain molecules, and Λ^3 is the de Broglie volume which incorporates all of the translational, rotational, and vibrational kinetic contributions of the molecule.

A2. Monomer Contribution

The monomer contribution for a molecule composed of m_s segments is

$$a^{MONO} = m_s a^M \tag{13}$$

where $a^M = A^M/(N_s k_B T)$ is the residual Helmholtz free energy per monomer, and N_s is the number of spherical segments. This term is expressed as a series expansion in the inverse of the temperature $\beta = 1/(k_BT)$ up to third-order:[86]

$$a^M = a^{HS} + \beta a_1 + \beta^2 a_2 + \beta^3 a_3 \tag{14}$$

In this relation, a^{HS} is the Helmholtz free energy of the reference hard-sphere (HS) fluid of diameter d, which is obtained from the Carnahan and Starling relation as[133]

$$a^{HS} = \frac{4\eta - 3\eta^2}{(1-\eta)^2} \tag{15}$$

where $\eta = (\pi/6)\rho_s d^3$, and $\rho_s = N_s/V$ is the number density of spherical segments. According to the theory of Barker and Henderson,[86] the effective diameter d can be obtained as

$$d = \int_0^\sigma [1 - \exp(-\beta u^{Mie}(r))]\, dr \tag{16}$$

The first perturbation term a_1 can be obtained with the following compact expression:

$$a_1 = C[x_0^{\lambda_a}\{a_1^s(\eta; \lambda_a) + B(\eta; \lambda_a)\} - x_0^{\lambda_r}\{a_1^s(\eta; \lambda_r) + B(\eta; \lambda_r)\}] \tag{17}$$

where $x_0 = \sigma/d$, C is the coefficient of the Mie potential defined in eq 2, and

$$B(\eta; \lambda) = 12\eta\varepsilon\left(\frac{1 - \eta/2}{(1-\eta)^3} I_\lambda(\lambda) - \frac{9\eta(1+\eta)}{2(1-\eta)^3} J_\lambda(\lambda)\right) \tag{18}$$

Note that in order to calculate the first- (and second-) order terms, as given by eq 17 (and eq 24 below), one needs to obtain an analytical expression for the mean-attractive energy $a_1^S(\lambda)$ of a Sutherland potential of variable range. This expression is obtained using a SAFT-VR[61,62] treatment which leads to the following compact expression:

$$a_1^s(\lambda) = -12\varepsilon\eta\left(\frac{1}{\lambda - 3}\right)\frac{1 - \eta_{eff}/2}{(1-\eta_{eff})^3} \tag{19}$$

where the effective packing fraction η_{eff} is parameterized for the range $5 < \lambda \leq 100$. The mean-attractive energy $a_1^S(\lambda)$ calculated in this way is as accurate as computer simulation results,[66] with the effective density correlated as

$$\eta_{eff} = c_1\eta + c_2\eta^2 + c_3\eta^3 + c_4\eta^4 \tag{20}$$

where the coefficients can be obtained from

$$\begin{pmatrix} c_1 \\ c_2 \\ c_3 \\ c_4 \end{pmatrix} = \begin{pmatrix} 0.81096 & 1.7888 & -37.578 & 92.284 \\ 1.0205 & -19.341 & 151.26 & -463.50 \\ -1.9057 & 22.845 & -228.14 & 973.92 \\ 1.0885 & -6.1962 & 106.98 & -677.64 \end{pmatrix} \begin{pmatrix} 1 \\ 1/\lambda \\ 1/\lambda^2 \\ 1/\lambda^3 \end{pmatrix} \tag{21}$$

In eq 18 the functions I_λ and J_λ are two integrals that depend on the parameters of the Mie potential, and are given by

$$I_\lambda(\lambda) = \int_1^{x_0} \frac{x^2}{x^\lambda} dx = -\frac{(x_0)^{-\lambda+3} - 1}{\lambda - 3} \tag{22}$$

and

$$J_\lambda(\lambda) = \int_1^{x_0} \frac{(x^3 - x^2)}{x^\lambda} dx = -\frac{(x_0)^{-\lambda+4}(\lambda - 3) - (x_0)^{-\lambda+3}(\lambda - 4) - 1}{(\lambda - 3)(\lambda - 4)} \tag{23}$$

The second-order perturbation term a_2 is evaluated with a modified macroscopic compressibility approximation (MCA)[66] which can be written as a function of the mean-attractive energies of hard-core Sutherland potentials a_1^S as

dx.doi.org/10.1021/jp306442b | J. Phys. Chem. B 2013, 117, 2717−2733

$$a_2 = \frac{1}{2}K^{HS}(1+\chi)\varepsilon C^2[x_0^{2\lambda_a}\{a_1^s(\eta; 2\lambda_a) + B(\eta; 2\lambda_a)\} - 2x_0^{(\lambda_a+\lambda_r)}\{a_1^s(\eta; \lambda_a+\lambda_r) + B(\eta; \lambda_a+\lambda_r)\} + x_0^{2\lambda_r}\{a_1^s(\eta; 2\lambda_r) + B(\eta; 2\lambda_r)\}] \quad (24)$$

where K^{HS} is the isothermal compressibility which is consistent with the Carnahan and Starling[133] expression

$$K^{HS} = \frac{(1-\eta)^4}{1+4\eta+4\eta^2-4\eta^3+\eta^4} \quad (25)$$

and χ is an empirical function of η introduced in order to reproduce the fluctuation term of the Mie potential obtained from Monte Carlo simulation.[66] This correction factor is expressed as

$$\chi = f_1(\alpha)\eta x_0^3 + f_2(\alpha)(\eta x_0^3)^5 + f_3(\alpha)(\eta x_0^3)^8 \quad (26)$$

where α represents the reduced attractive van der Waals constant of the Mie potential

$$\alpha = C\left(\frac{1}{\lambda_a-3} - \frac{1}{\lambda_r-3}\right) \quad (27)$$

The third-order term in the Helmholtz free energy expansion is expressed as the empirical function

$$a_3 = -\varepsilon^3 f_4(\alpha)\eta x_0^3 \exp(f_5(\alpha)\eta x_0^3 + f_6(\alpha)\eta^2 x_0^6) \quad (28)$$

which depends on the Mie exponents λ_a and λ_r through the constant α. The functions f_i are defined as

$$f_i(\alpha) = \sum_{n=0}^{n=3}\phi_{i,n}\alpha^n \Big/ \left(1 + \sum_{n=4}^{n=6}\phi_{i,n}\alpha^{n-3}\right) \quad \text{for} \quad i = 1, ..., 6 \quad (29)$$

The values of the coefficients $\phi_{i,n}$ are reported in Table 3.

A3. Chain Contribution

Assuming that the segments are bonded together at $r = \sigma$, i.e., that the model consists of freely jointed chains of tangent segments, the residual contribution to the Helmholtz free energy can be expressed as

$$a^{CHAIN} = -(m_s - 1)\ln g^{Mie}(\sigma) \quad (30)$$

where $g^{Mie}(\sigma)$ is the contact value of the radial distribution function (RDF) of the monomer Mie fluid, which is obtained from the following expression:[66]

$$g^{Mie}(\sigma) = g_d^{HS}(\sigma)\exp(\beta\varepsilon g_1(\sigma)/g_d^{HS}(\sigma) + (\beta\varepsilon)^2 g_2(\sigma)/g_d^{HS}(\sigma)) \quad (31)$$

where $g_d^{HS}(\sigma)$ refers to the RDF of a fluid of hard spheres of diameter d evaluated at diameter σ. This is obtained using the expression of Boublík[134]

$$g_d^{HS}(x_0) = \exp(k_0 + k_1 x_0 + k_2 x_0^2 + k_3 x_0^3) \quad (32)$$

where $x_0 = \sigma/d$. In this expression, the density-dependent coefficients k_i are given by

$$k_0 = -\ln(1-\eta) + \frac{42\eta - 39\eta^2 + 9\eta^3 - 2\eta^4}{6(1-\eta)^3} \quad (33)$$

$$k_1 = \frac{(\eta^4 + 6\eta^2 - 12\eta)}{2(1-\eta)^3} \quad (34)$$

$$k_2 = \frac{-3\eta^2}{8(1-\eta)^2} \quad (35)$$

$$k_3 = \frac{(-\eta^4 + 3\eta^2 + 3\eta)}{6(1-\eta)^3} \quad (36)$$

The first-order term in the expansion for the contact value of the radial distribution function in eq 31 is expressed in terms of the first-order perturbation terms of the Helmholtz free energy of Sutherland (a_1^s) and Mie (a_1) potentials as follows:

$$g_1(\sigma) = \frac{1}{2\pi\varepsilon d^3}\left[3\frac{\partial a_1}{\partial \rho_s} - C\lambda_a x_0^{\lambda_a}\frac{a_1^s(\eta; \lambda_a) + B(\eta; \lambda_a)}{\rho_s} + C\lambda_r x_0^{\lambda_r}\frac{a_1^s(\eta; \lambda_r) + B(\eta; \lambda_r)}{\rho_s}\right] \quad (37)$$

The second-order term in the expansion of the contact value of the radial distribution function is based on a corrected MCA approximation

$$g_2(\sigma) = (1+\gamma_c)g_2^{MCA}(\sigma) \quad (38)$$

where

$$g_2^{MCA}(\sigma) = \frac{1}{2\pi\varepsilon^2 d^3}\left[3\frac{\partial}{\partial\rho_s}\left(\frac{a_2}{1+\chi}\right) - \varepsilon K^{HS}C^2\lambda_r x_0^{2\lambda_r}\frac{a_1^s(\eta; 2\lambda_r) + B(\eta; 2\lambda_r)}{\rho_s} + \varepsilon K^{HS}C^2(\lambda_r+\lambda_a)x_0^{\lambda_r+\lambda_a}\frac{a_1^s(\eta; \lambda_r+\lambda_a) + B(\eta; \lambda_r+\lambda_a)}{\rho_s} - \varepsilon K^{HS}C^2\lambda_a x_0^{2\lambda_a}\frac{a_1^s(\eta; 2\lambda_a) + B(\eta; 2\lambda_a)}{\rho_s}\right] \quad (39)$$

The form of the empirical correction factor γ_c is chosen in order to capture the positive slope of the radial distribution function at contact for long-range Mie potentials at low temperature and low density. The correction factor depends on both the density and temperature as well as the Mie exponents (λ_a,λ_r) through

$$\gamma_c = \phi_{7,0}(-\tanh(\phi_{7,1}(\phi_{7,2} - \alpha)) + 1)\eta x_0^3\theta \exp(\phi_{7,3}\eta x_0^3 + \phi_{7,4}\eta^2 x_0^6) \quad (40)$$

where $\theta = \exp(\beta\varepsilon) - 1$, α is given by eq 27, and the values of $\phi_{7,i}$ are reported in Table 3.

AUTHOR INFORMATION

Corresponding Author

*E-mail: g.jackson@imperial.ac.uk.

Notes

The authors declare no competing financial interest.

ACKNOWLEDGMENTS

C.A. and T.L. are very grateful to the Engineering and Physical Sciences Research Council (EPSRC) of the UK for the award

of postdoctoral fellowships. Additional funding to the Molecular Systems Engineering Group from the EPSRC (grants GR/T17595, GR/N35991, and EP/E016340), the Joint Research Equipment Initiative (JREI) (GR/M94426), and the Royal Society-Wolfson Foundation refurbishment scheme is also gratefully acknowledged. The simulations were performed using the facilities of the Imperial College High Performance Computing Service.

REFERENCES

(1) de Pablo, J. J.; Escobedo, F. A. *AIChE J.* **2002**, *48*, 2716−2721.
(2) Maginn, E. J. *AIChE J.* **2009**, *55*, 1304−1310.
(3) Gubbins, K. E.; Moore, J. D. *Ind. Eng. Chem. Res.* **2010**, *49*, 3026−3046.
(4) Theodorou, D. N. *Ind. Eng. Chem. Res.* **2010**, *49*, 3047−3058.
(5) Leach, A. R. *Molecular modelling: Principles and Applications*, 2nd ed.; Prentice-Hall: Harlow, 2001.
(6) Schmidt, J.; VandeVondele, J.; Kuo, I. F. W.; Sebastiani, D.; Siepmann, J. I.; Hutter, J.; Mundy, C. J. *J. Phys. Chem. B* **2009**, *113*, 11959−11964.
(7) Lin, I.-C.; Seitsonen, A. P.; Coutinho-Neto, M. D.; Tavernelli, I.; Rothlisberger, U. *J. Phys. Chem. B* **2009**, *113*, 1127−1131.
(8) Weber, V.; Asthagiri, D. *J. Chem. Phys.* **2010**, *133*, 141101.
(9) Kühne, T. D.; Pascal, T. A.; Kaxiras, E.; Jung, Y. *J. Phys. Chem. Lett.* **2011**, *2*, 105−113.
(10) Balasubramanian, S.; Kohlmeyer, A.; Klein, M. L. *J. Chem. Phys.* **2009**, *131*, 144506.
(11) McGrath, M. J.; Kuo, I.-F. W.; Ghogomu, J. N.; Mundy, C. J.; Siepmann, J. I. *J. Phys. Chem. B* **2011**, *115*, 11688−11692.
(12) Hill, T. L. *Statistical Mechanics*; McGraw-Hill: New York, 1956.
(13) McQuarrie, D. A. *Statistical Mechanics*; Harper & Row: New York, 1976.
(14) Allen, M. P.; Tildesley, D. J. *Computer Simulation of Liquids*; Oxford University Press: Oxford, 1987.
(15) Frenkel, D.; Smit, B. *Understanding Molecular Simulation*, 2nd ed.; Academic Press: London, 2002.
(16) Rapaport, D. C. *The Art of Molecular Dynamics Simulation*, 2nd ed.; Cambridge University Press, 2004.
(17) Landau, D. P.; Binder, K. *A Guide to Monte Carlo Simulations in Statistical Physics*, 2nd ed.; Cambridge University Press, 2005.
(18) Ungerer, P.; Tavitian, B.; Boutin, A. *Applications of Molecular Simulation in the Oil and Gas Industry*; Editions Technip, 2005.
(19) Nielsen, S. O.; López, C. F.; Srinivas, G.; Klein, M. L. *J. Phys. Condes. Matter* **2004**, *16*, R481−R512.
(20) Klein, M. L.; Shinoda, W. *Science* **2008**, *321*, 798−800.
(21) Müller-Plathe, F. *Chem. Phys. Chem.* **2002**, *3*, 754−769.
(22) Faller, R. *Phys. Chem. Chem. Phys.* **2009**, *11*, 1867−1868.
(23) Peter, C.; Kremer, K. *Soft Matter* **2009**, *5*, 4357−4366.
(24) Voth, G. A. *Coarse-Graining of Condensed Phase and Biomolecular Systems*; CRC Press, 2009.
(25) Peter, C.; Kremer, K. *Faraday Discuss.* **2010**, *144*, 9−24.
(26) Noid, W. G.; Chu, J.-W.; Ayton, G. S.; Krishna, V.; Izvekov, S.; Voth, G. A.; Das, A.; Andersen, H. C. *J. Chem. Phys.* **2008**, *128*, 244114.
(27) Reith, D.; Pütz, M.; Müller-Plathe, F. *J. Comput. Chem.* **2003**, *24*, 1624−1636.
(28) Lyubartsev, A. P.; Laaksonen, A. *Phys. Rev. E* **1995**, *52*, 3730−3737.
(29) Izvekov, S.; Parrinello, M.; Burnham, C. J.; Voth, G. A. *J. Chem. Phys.* **2004**, *120*, 10896.
(30) Izvekov, S.; Voth, G. A. *J. Chem. Phys.* **2005**, *123*, 134105.
(31) Izvekov, S.; Voth, G. A. *J. Phys. Chem. B* **2005**, *109*, 2469−2473.
(32) Henderson, R. L. *Phys. Lett. A* **1974**, *49*, 197−198.
(33) Gray, C. G.; Gubbins, K. E. *Theory of Molecular Fluids*; Clarendon Press: Oxford, 1984; Vol. *1*.
(34) Shell, M. S. *J. Chem. Phys.* **2008**, *129*, 144108.
(35) Chaimovich, A.; Shell, M. S. *Phys. Chem. Chem. Phys.* **2009**, *11*, 1901−1915.
(36) Marrink, S. J.; Risselada, H. J.; Yefimov, S.; Tieleman, D. P.; de Vries, A. H. *J. Phys. Chem. B* **2007**, *111*, 7812−7824.
(37) Shelley, J. C.; Shelley, M. Y.; Reeder, R. C.; Bandyopadhyay, S.; Klein, M. L. *J. Phys. Chem. B* **2001**, *105*, 4464−4470.
(38) Nielsen, S. O.; Lopez, C. F.; Srinivas, G.; Klein, M. L. *J. Chem. Phys.* **2003**, *119*, 7043.
(39) Shinoda, W.; DeVane, R.; Klein, M. L. *Mol. Simul.* **2007**, *33*, 27−36.
(40) DeVane, R.; Shinoda, W.; Moore, P. B.; Klein, M. L. *J. Chem. Theory Comput.* **2009**, *5*, 2115−2124.
(41) Chiu, S.-W.; Scott, H. L.; Jakobsson, E. *J. Chem. Theory Comput.* **2010**, *6*, 851−863.
(42) Maerzke, K. A.; Siepmann, J. I. *J. Phys. Chem. B* **2011**, *115*, 3452−3465.
(43) Jones, J. E. *Proc. R. Soc. London, Ser. A: Math. Phys. Eng. Sci.* **1924**, *106*, 463−477.
(44) Lennard-Jones, J. E. *Proc. Phys. Soc. London* **1931**, *43*, 461−482.
(45) Morse, P. M. *Phys. Rev.* **1929**, *34*, 57−64.
(46) Mie, G. *Ann. Phys.* **1903**, *316*, 657−697.
(47) Avendaño, C.; Lafitte, T.; Galindo, A.; Adjiman, C. S.; Jackson, G.; Müller, E. A. *J. Phys. Chem. B* **2011**, *115*, 11154−11169.
(48) Chapman, W. G.; Gubbins, K. E.; Jackson, G.; Radosz, M. *Fluid Phase Equilib.* **1989**, *52*, 31−38.
(49) Chapman, W. G.; Gubbins, K. E.; Jackson, G.; Radosz, M. *Ind. Eng. Chem. Res.* **1990**, *29*, 1709−1721.
(50) Wertheim, M. S. *J. Stat. Phys.* **1984**, *35*, 19−34.
(51) Wertheim, M. S. *J. Stat. Phys.* **1984**, *35*, 35−47.
(52) Wertheim, M. S. *J. Stat. Phys.* **1986**, *42*, 459−476.
(53) Wertheim, M. S. *J. Stat. Phys.* **1986**, *42*, 477−492.
(54) Wertheim, M. S. *J. Chem. Phys.* **1986**, *85*, 2929−2936.
(55) Wertheim, M. S. *J. Chem. Phys.* **1987**, *87*, 7323−7331.
(56) Chapman, W. G.; Jackson, G.; Gubbins, K. E. *Mol. Phys.* **1988**, *65*, 1057−1079.
(57) Müller, E. A.; Gubbins, K. E. *Ind. Eng. Chem. Res.* **2001**, *40*, 2193−2211.
(58) Economou, I. G. *Ind. Eng. Chem. Res.* **2002**, *41*, 953−962.
(59) Tan, S. P.; Adidharma, H.; Radosz, M. *Ind. Eng. Chem. Res.* **2008**, *47*, 8063−8082.
(60) McCabe, C.; Galindo, A. In *Applied Thermodynamics of Fluids*; Goodwin, A. R., Sengers, J., Peters, C. J., Eds.; Royal Society of Chemistry, London, 2010; Chapter 8
(61) Gil-Villegas, A.; Galindo, A.; Whitehead, P. J.; Mills, S. J.; Jackson, G.; Burgess, A. N. *J. Chem. Phys.* **1997**, *106*, 4168−4186.
(62) Galindo, A.; Davies, L. A.; Gil-Villegas, A.; Jackson, G. *Mol. Phys.* **1998**, *93*, 241−252.
(63) Davies, L. A.; Gil-Villegas, A.; Jackson, G. *Int. J. Thermophys.* **1998**, *19*, 675−686.
(64) Davies, L. A.; Gil-Villegas, A.; Jackson, G. *J. Chem. Phys.* **1999**, *111*, 8659−8665.
(65) Lafitte, T.; Bessieres, D.; Piñeiro, M. M.; Daridon, J.-L. *J. Chem. Phys.* **2006**, *124*, 024509.
(66) Lafitte, T.; Apostolakou, A.; Avendaño, C.; Galindo, A.; Adjiman, C. S.; Müller, E. A.; Jackson, G. Submitted, 2013
(67) Lymperiadis, A.; Adjiman, C. S.; Galindo, A.; Jackson, G. *J. Chem. Phys.* **2007**, *127*, 234903.
(68) Lymperiadis, A.; Adjiman, C. S.; Jackson, G.; Galindo, A. *Fluid Phase Equilib.* **2008**, *274*, 85−104.
(69) Papaioannou, V.; Lafitte, T.; Avendano, C.; Adjiman, C. S.; Jackson, G.; Müller, E. A.; Galindo, A. In preparation, 2013
(70) Müller, E. A.; Gubbins, K. E. *Ind. Eng. Chem. Res.* **1995**, *34*, 3662−3673.
(71) Stell, G.; Rasaiah, J. C.; Narang, H. *Mol. Phys.* **1974**, *27*, 1393−1414.
(72) van Westen, T.; Vlugt, T. J. H.; Gross, J. *J. Phys. Chem. B* **2011**, *115*, 7872−7880.
(73) Gross, J.; Sadowski, G. *Ind. Eng. Chem. Res.* **2001**, *40*, 1244−1260.
(74) Martin, M. G.; Siepmann, J. I. *J. Phys. Chem. B* **1998**, *102*, 2569−2577.

(75) Potoff, J. J.; Bernard-Brunel, D. A. *J. Phys. Chem. B* **2009**, *113*, 14725−14731.
(76) Du, Q.; Yang, Z.; Yang, N.; Yang, X. *Ind. Eng. Chem. Res.* **2010**, *49*, 8271−8278.
(77) Søndergaard, R.; Nielsen, O. J.; Hurley, M. D.; Wallington, T. J.; Singh, R. *Chem. Phys. Lett.* **2007**, *443*, 199−204.
(78) Gordon, P. A. *J. Chem. Phys.* **2006**, *125*, 014504.
(79) He, X.; Shinoda, W.; DeVane, R.; Klein, M. L. *Mol. Phys.* **2010**, *108*, 2007−2020.
(80) Shinoda, W.; DeVane, R.; Klein, M. L. *J. Phys. Chem. B* **2010**, *114*, 6836−6849.
(81) DeVane, R.; Klein, M. L.; Chiu, C.-c.; Nielsen, S. O.; Shinoda, W.; Moore, P. B. *J. Phys. Chem. B* **2010**, *114*, 6386−6393.
(82) Shinoda, W.; DeVane, R.; Klein, M. L. In *Coarse-Graining of Condensed Phase and Biomolecular Systems*; Voth, G. A., Ed.; CRC Press, 2009; Chapter self assembly of surfactants in bulk phases and at interfaces using coarse-grain models.
(83) Galindo, A.; Gil-Villegas, A.; Jackson, G.; Burgess, A. N. *J. Phys. Chem. B* **1999**, *103*, 10272−10281.
(84) Gil-Villegas, A.; Galindo, A.; Jackson, G. *Mol. Phys.* **2001**, *99*, 531−546.
(85) Lemmon, E. W.; McLinden, M. O.; Friend, D. G. In *NIST Chemistry WebBook, NIST Standard Reference Database, Number 69*; Linstrom, P. J., Mallard, W. G., Eds.; Chapter Thermophysical Properties of Fluid Systems; http://webbook.nist.gov/chemistry/fluid/.
(86) Barker, J. A.; Henderson, D. *Rev. Mod. Phys.* **1976**, *48*, 587−671.
(87) Müller, E. A.; Gubbins, K. E.; Tsangaris, D. M.; de Pablo, J. J. *J. Chem. Phys.* **1995**, *103*, 3868−3869.
(88) Nosé, S. *J. Chem. Phys.* **1984**, *81*, 511−519.
(89) Hoover, W. G. *Phys. Rev. A* **1985**, *31*, 1695−1697.
(90) Ryckaert, J. P.; Ciccotti, G.; Berendsen, H. J. C. *J. Comput. Phys.* **1977**, *23*, 327−341.
(91) Smith, W. *Mol. Simul.* **2006**, *32*, 933.
(92) Trokhymchuk, A.; Alejandre, J. *J. Chem. Phys.* **1999**, *111*, 8510−8523.
(93) Chapela, G. A.; Saville, G.; Rowlinson, J. S. *Faraday Discuss. Chem. Soc.* **1975**, *59*, 22−28.
(94) Chapela, G. A.; Saville, G.; Thompson, S. M.; Rowlinson, J. S. *J. Chem Soc., Faraday Trans.* **1977**, *73*, 1133−1144.
(95) Martínez-Veracoechea, F.; Müller, E. A. *Mol. Simul.* **2005**, *31*, 33−43.
(96) Siepmann, J. I. Private communication, 2012
(97) Gelb, L. D.; Müller, E. A. *Fluid Phase Equilib.* **2002**, *203*, 1−14.
(98) Noya, E. G.; Vega, C.; de Miguel, E. *J. Chem. Phys.* **2008**, *128*, 154507.
(99) Müller, E. A.; Mejía, A. *Fluid Phase Equilib.* **2009**, *282*, 68−81.
(100) Rowlinson, J. S.; Widom, B. *Molecular Theory of Capillarity*; Clarendon: Oxford, 1982.
(101) de Miguel, E.; Jackson, G. *J. Chem. Phys.* **2006**, *125*, 164109.
(102) de Miguel, E.; Jackson, G. *Mol. Phys.* **2006**, *104*, 3717−3734.
(103) Wegner, F. J. *Phys. Rev. B* **1972**, *5*, 4529−4536.
(104) Vega, L.; de Miguel, E.; Rull, L. F.; Jackson, G.; McLure, I. A. *J. Chem. Phys.* **1992**, *96*, 2296−2305.
(105) Lagache, M.; Ungerer, P.; Boutin, A.; Fuchs, A. H. *Phys. Chem. Chem. Phys.* **2001**, *3*, 4333−4339.
(106) Colina, C. M.; Olivera-Fuentes, C. G.; Siperstein, F. R.; Lísal, M.; Gubbins, K. E. *Mol. Simul.* **2003**, *29*, 405−412.
(107) Lagache, M. H.; Ungerer, P.; Boutin, A. *Fluid Phase Equilib.* **2004**, *220*, 211−223.
(108) Guggenheim, E. A. *J. Chem. Phys.* **1945**, *13*, 253−261.
(109) Müller, E. A.; Gelb, L. D. *Ind. Eng. Chem. Res.* **2003**, *42*, 4123−4131.
(110) Errington, J. R. *J. Chem. Phys.* **2003**, *118*, 9915−9925.
(111) Errington, J. R. *Phys. Rev. E* **2003**, *67*, 012102.
(112) Potoff, J. J.; Panagiotopoulos, A. Z. *J. Chem. Phys.* **1998**, *109*, 10914−10920.
(113) Kiselev, S. B.; Ely, J. F.; Adidharma, H.; Radosz, M. *Fluid Phase Equilib.* **2001**, *183*, 53−64.
(114) McCabe, C.; Kiselev, S. B. *Fluid Phase Equilib.* **2004**, *219*, 3−9.
(115) Llovell, F.; Pamies, J. C.; Vega, L. F. *J. Chem. Phys.* **2004**, *121*, 10715−10724.
(116) Bymaster, A.; Emborsky, C.; Dominik, A.; Chapman, W. G. *Ind. Eng. Chem. Res.* **2008**, *47*, 6264−6274.
(117) Tang, X.; Gross, J. *J. Supercrit. Fluids* **2010**, *55*, 735−742.
(118) Forte, E.; Llovell, F.; Vega, L. F.; Trusler, J. P. M.; Galindo, A. *J. Chem. Phys.* **2011**, *134*, 154102.
(119) Raabe, G.; Maginn, E. J. *J. Phys. Chem. Lett.* **2010**, *1*, 93−96.
(120) Raabe, G.; Maginn, E. J. *J. Phys. Chem. B* **2010**, *114*, 10133−10142.
(121) Paulechka, E.; Kazakov, A.; Frenkel, M. *Int. J. Thermophys.* **2010**, *31*, 462−474.
(122) Tanaka, K.; Higashi, Y. Physical Properties of HFO-1234yf; Third IIR Conference on Thermophysical Properties and Transfer Processes of Refrigerants; Boulder, CO; June 23−26, 2009.
(123) Tanaka, K.; Higashi, Y. *Int. J. Refrig.* **2010**, *33*, 474−479.
(124) Gil-Villegas, A.; McGrother, S. C.; Jackson, G. *Mol. Phys.* **1997**, *92*, 723−734.
(125) Avendaño, C.; Gil-Villegas, A. *Mol. Phys.* **2006**, *104*, 1475−1486.
(126) Vargaftik, N. B. *Moskva* **1972**, 156.
(127) Liessmann, G.; Schmidth, W.; Reiffarth, S. *Data compilation of the Saechsische Olefinwerke Boehlen Germany* **1995**, 1.
(128) Müller, E. A.; Mejía, A. *J. Phys. Chem. B* **2011**, *115*, 12822−12834.
(129) Smit, B.; Karaborni, S.; Siepmann, J. I. *J. Chem. Phys.* **1995**, *102*, 2126−2140.
(130) Smit, B.; Karaborni, S.; Siepmann, J. I. *J. Chem. Phys.* **1998**, *109*, 352.
(131) Nath, S. K.; Escobedo, F. A.; de Pablo, J. J. *J. Chem. Phys.* **1998**, *108*, 9905−9911.
(132) Lafitte, T.; Avendaño, C.; Papaioannou, V.; Galindo, A.; Adjiman, C. S.; Jackson, G.; Müller, E. A. *Mol. Phys.* **2012**, *110*, 1189−1203.
(133) Carnahan, N. F.; Starling, K. E. *J. Chem. Phys.* **1969**, *51*, 635−636.
(134) Boublík, T. *Mol. Phys.* **1986**, *59*, 775−793.